

# The spectacular evolution of Supernova 1996al over 15 years: a low energy explosion of a stripped massive star in a highly structured environment

S. Benetti<sup>1</sup>, N. N. Chugai<sup>2</sup>, V. P. Utrobin<sup>3</sup>, E. Cappellaro<sup>1</sup>, F. Patat<sup>4</sup>, A. Pastorello<sup>1</sup>, M. Turatto<sup>1</sup>, G. Cupani<sup>5</sup>, R. Neuhäuser<sup>6</sup>, N. Caldwell<sup>7</sup>, G. Pignata<sup>8,9</sup>, L. Tomasella<sup>1</sup>

<sup>1</sup>*INAF - Osservatorio Astronomico di Padova, vicolo dell'Osservatorio 5, I-35122 Padova, Italy*

<sup>2</sup>*Institute of Astronomy of Russian Academy of Sciences, Pyatnitskaya St. 48, 119017 Moscow, Russia*

<sup>3</sup>*Institute of Theoretical and Experimental Physics, B. Chermushkinskaya St. 25, 117218 Moscow, Russia*

<sup>4</sup>*European Southern Observatory, Karl-Schwarzschild-Str. 2, D-85748 Garching bei München, Germany*

<sup>5</sup>*INAF - Osservatorio Astronomico di Trieste, Via G.B. Tiepolo, 11 I-34131 Trieste, Italy*

<sup>6</sup>*Astrophysikalisches Institut und Universitäts-Sternwarte, FSU Jena, Schillergäßchen 2-3, D-07745 Jena, Germany*

<sup>7</sup>*Harvard-Smithsonian Center for Astrophysics, Cambridge, MA 02138, USA*

<sup>8</sup>*Departamento de Ciencias Físicas, Universidad Andres Bello, Avda. Republica 252, Santiago, Chile*

<sup>9</sup>*Millennium Institute of Astrophysics, Chile*

Received .....; accepted .....

## ABSTRACT

Spectrophotometry of SN 1996al carried out throughout 15 years is presented. The early photometry suggests that SN 1996al is a Linear type-II supernova, with an absolute peak of  $M_V \sim -18.2$  mag. Early spectra present broad, asymmetric Balmer emissions, with super-imposed narrow lines with P-Cygni profile, and He I features with asymmetric, broad emission components. The analysis of the line profiles shows that the H and He broad components form in the same region of the ejecta. By day +142, the H $\alpha$  profile dramatically changes: the narrow P-Cygni profile disappears, and the H $\alpha$  is fitted by three emission components, that will be detected over the remaining 15 yrs of the SN monitoring campaign. Instead, the He I emissions become progressively narrower and symmetric. A sudden increase in flux of all He I lines is observed between 300 and 600 days. Models show that the supernova luminosity is sustained by the interaction of low mass ( $\sim 1.15 M_\odot$ ) ejecta, expelled in a low kinetic energy ( $\sim 1.6 \times 10^{50}$  erg) explosion, with highly asymmetric circumstellar medium. The detection of H $\alpha$  emission in pre-explosion archive images suggests that the progenitor was most likely a massive star ( $\sim 25 M_\odot$  ZAMS) that had lost a large fraction of its hydrogen envelope before explosion, and was hence embedded in a H-rich cocoon. The low-mass ejecta and modest kinetic energy of the explosion are explained with massive fallback of material into the compact remnant, a  $7 - 8 M_\odot$  black hole.

**Key words:** Supernovae: general – Supernovae: 1996al

## 1 INTRODUCTION

The aftermath of a supernova explosion is a bubble of gas expanding at very high velocity. Eventually, the ejecta may impact on the pre-existing circumstellar material (CSM), generating a shock in which a fraction of the kinetic energy of the ejecta is converted into radiation. The intensity of the resulting emission mostly depends on the density of the CSM and the velocity contrast between the ejecta and the CSM. If the density of the CSM is low, the emission from the CSM-ejecta interaction becomes visible only after the SN luminosity has faded, sometimes several years after the

explosion. However, occasionally, the CSM near the SN is so dense that the CSM-ejecta interaction dominates the SN emission even at early phases.

With improved statistics and quality of observations, we are now observing counterparts for the different scenarios, and a new taxonomy for type II supernovae (SNII), based on the mass of the residual hydrogen envelope and the strength of the CSM-ejecta interaction signatures, can be proposed. The emission of classical SNII is determined by the thermal balance in the ejecta, and CSM-ejecta interaction is negligible (at least at early phases). Depending on the shape

of the light curve, they are sub-classified into plateau (IIP) and linear (IIL) types. The current interpretation is that different light curves correspond to different envelope masses, ranging from  $\sim 10 M_{\odot}$  in SNIIP (cf. Smartt 2009) to  $\sim 1 M_{\odot}$  in SNIIL, due to different progenitor initial masses and mass loss histories. When soon after the explosion the SN ejecta interact with a dense CSM, the SN emission itself is overwhelmed by the emission arising from the interaction (Chugai 1990; Chevalier & Fransson 1994; Terlevich 1994). Best examples of this class are SN 1988Z (Turatto et al. 1993; Aretxaga et al. 1999), with a long plateau-like light curve, and SN 1998S (Liu et al. 2000; Fassia et al. 2000) with a linear-like light curve. These SNe are named as type IIn.

In some SNII, the CSM-ejecta interaction contribution emerges only when the  $^{56}\text{Co}$  decay energy input fades. The fact that these are mostly SNIIL is consistent with our understanding that they experienced stronger mass loss during their evolutions (e.g. SNe 1980K, 1979C, and 1990K; Uomoto & Kirshner 1986; Fesen et al. 1999; Cappellaro et al. 1995, respectively), hence they are expected to have higher CSM density.

Somewhat in between, a few SNe have emission line profiles which reveal the presence of a CSM around the exploding stars from early-on, though the ejecta-CSM interaction becomes preponderant some months later. These are sometimes labeled SNIId, where 'd' stands for 'double' profile because of the simultaneous presence of broad profiles from the ejecta and narrow ones from the CSM. SN 1994aj (Benetti et al. 1998, Paper I) and SN 1996L (Benetti et al. 1999, Paper II) belong to this group.

In this paper we present the study of a new SN (SN 1996al) with spectroscopic properties very similar to those of SNIId (Benetti & Neuhauser 1996). SN 1996al was visually discovered on July 22.71 UT by Evans et al. (1996), about  $30''$  north of the center of its host galaxy, NGC 7689. The measured position of the SN is R.A. =  $23^{\text{h}}33^{\text{m}}16^{\text{s}}.29 \pm 0.03$ ; Decl. =  $-54^{\circ}04'59''.69 \pm 0.05$  (J2000.0), in agreement with that reported by Evans et al. (1996).

In view of its relative closeness and apparent brightness, an extensive observational campaign was set-up with the ESO-Chile telescopes. Thanks to this massive effort, we have been able to follow the SN for more than 15 years, and it has become one of the best monitored SNIIL-SNIId.

In this paper we will describe the physical properties of the explosion and constrain the nature of SN 1996al progenitor star.

## 2 OBSERVATIONS

Spectroscopy and imaging observations were carried out at ESO La Silla and Paranal Observatories using a number of different telescopes and/or instruments (see Tables A1 & A2).

### 2.1 Optical Photometry

The CCD frames were first bias and flat-field corrected in a standard manner. Since a fraction of data was obtained under non-photometric conditions, relative photometry was

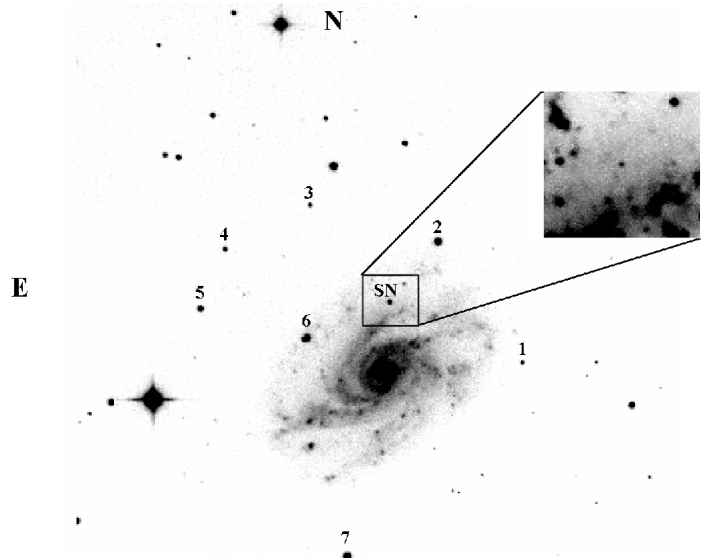


**Figure 1.** SN 1996al in NGC 7689 and reference stars. The main image is an  $R$  frame taken on 1996 October 1 with the D1.54m+DFOSC. The seeing is  $1.4''$  and the field of view is  $5.9' \times 5.9'$ . The zoomed image was obtained with VLT+FORIS2 using a redshifted  $H_{\alpha}$  filter on 2002 June 16. The seeing was  $0.7''$  and the field of view is  $25''$ . The SN is the source at the center of the image.

performed with respect to a local sequence of field stars (see Figure 1). Twelve photometric nights were used to calibrate this sequence against Landolt standard stars (Landolt 1992). The magnitudes and estimated errors of the local standards are shown in Table 1. These magnitudes were obtained by summing the counts through an aperture, whose size varied according to the seeing.

Ideally, one would like to remove the galaxy background by subtracting a galaxy “template” where the SN is absent. However, a suitable template image was not available. Therefore, the SN magnitudes were measured using the IRAF<sup>1</sup> point spread function fitting task Daophot (Stetson 1992) and/or ROMAFOT package (Buonanno et al. 1983) under MIDAS<sup>2</sup>. These procedures allowed the simultaneous fit and subtraction of the galaxy background. While the pixel scales changed from one instrument to another, they were always sufficiently small to provide good sampling of the PSF (see last column, and caption of Table A1). The supernova magnitudes with estimated internal errors are listed in Table A1, which also gives the seeing for each epoch, averaged over the observed bands.

On Dec. 8, 2007 an  $H_{\alpha}$  frame of SN 1996al was also secured with VLT+FORIS2, and the frame was calibrated observing in the same night the spectrophotometric standard G158-100 (Oke 1990). The derived  $H_{\alpha}$  flux inside the SN 1996al

<sup>1</sup> IRAF is distributed by the National Optical Astronomy Observatories, which are operated by the Association of Universities for Research in Astronomy, Inc., under cooperative agreement with the National Science Foundation.

<sup>2</sup> <https://www.eso.org/sci/software/esomidas/>

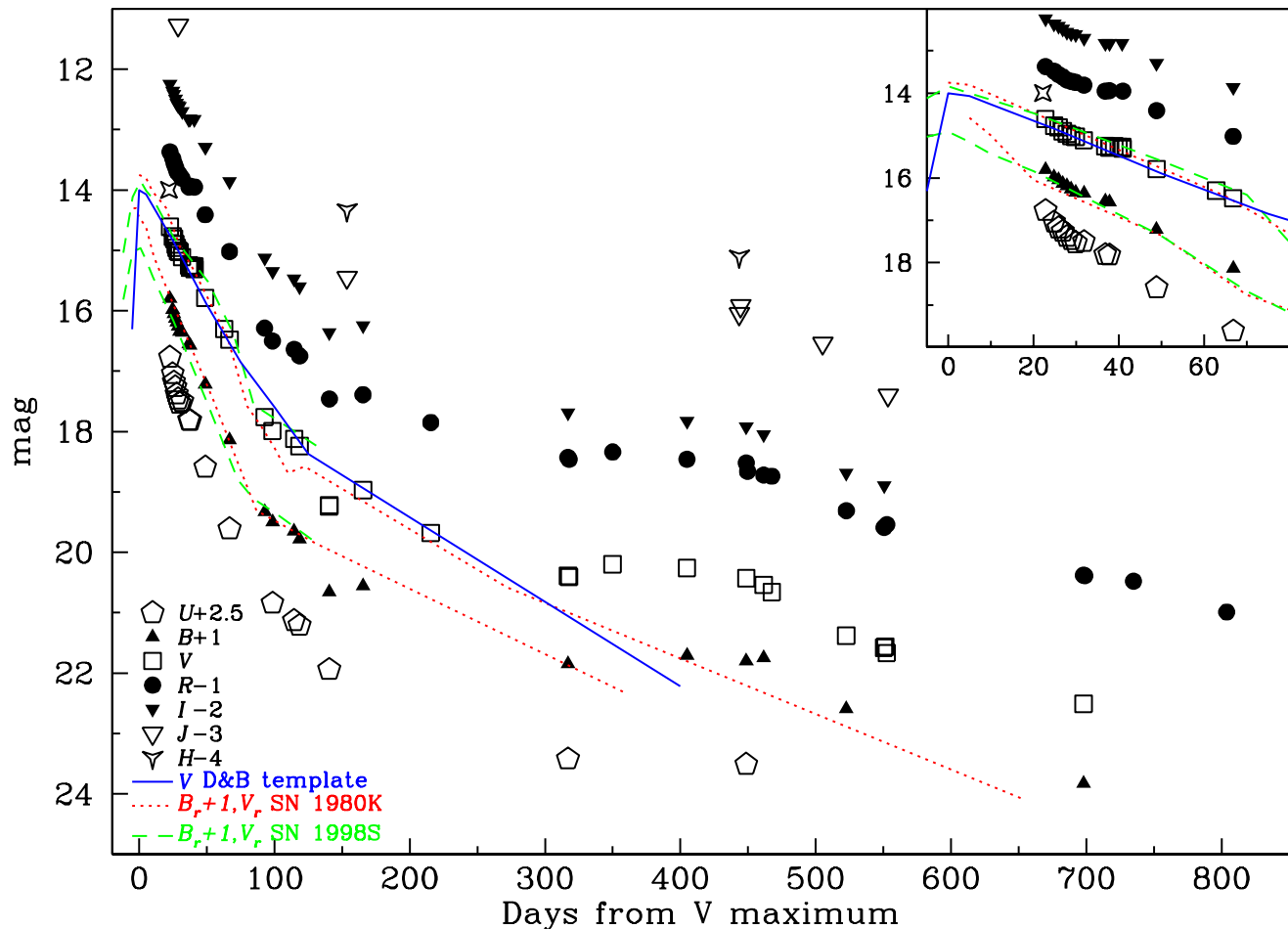


**Figure 2.**  $U, B, V, R, I, J$  and  $H$  light curves of SN 1996al. The *dotted* lines represent the  $B$  and  $V$  light curves of SN 1980K (Barbon et al. 1982; Buta 1982; Tsvetkov 1983). The distance to the SN 1980K host galaxy, NGC 6948, is taken from Karachentsev et al. (2000). The SN 1980K  $B, V$  light curves are reported to the distance and reddening of SN 1996al with a  $+0.3$  mag shift, and labelled  $B_r$  and  $V_r$  in the figure. The *dashed* lines represent the  $B$  and  $V$  light curves of SN 1998S (Liu et al. 2000; Fassia et al. 2000). The distance for the SN 1998S host galaxy, NGC 3877, is taken from Willick et al. (1997). The SN 1998S  $B, V$  light curves are reported to the distance and reddening of SN 1996al with a  $+1.5$  mag shift, and labelled  $B_r$  and  $V_r$  in the figure. The *starry* symbol is the visual SN estimate at the discovery from Evans et al. (1996). The best match with the template  $V$  light curve of SNIIL (from Doggett & Branch 1985), along with the comparisons with those of SNe 1980K and 1998S, suggest that the maximum occurred on MJD  $\sim 50265 \pm 2$  days at a magnitude  $V \sim 13.9 \pm 0.3$ .

PSF was found to be in excellent agreement with that derived from the subsequent FORS2 spectrum (Sect. 2.4).

### 2.1.1 Light curves

The  $UBVRIJH$  light curves are plotted in Figure 2. Patat et al. (1994) showed that SNIa can be characterised on the basis of the  $\beta_{100}$  parameter, which quantifies the luminosity decline rate in the first 100 days after maximum light. For SN 1996al, we measure  $\beta_{100}^B = 4.84 \text{ mag} (100\text{d})^{-1}$ , which is typical of the type IIL subclass, very similar for instance to SN 1980K. However, the post maximum decline

shows a short plateau-like break (see inset of Figure 2) in all bands. This flattening is reached at day  $+30$  in  $U$  and  $B$  bands, and is very short (2–3 days). In  $VRI$  it is reached a few days later ( $+34\text{d}$ ), and it lasts about one week.

The comparisons with the light curves of SNe 1980K and 1998S  $V$ , and the  $V$ -band template light curve of SNIIL from Doggett & Branch (1985), suggest that SN 1996al reaches the  $V$  maximum on MJD  $= 50265 \pm 2$  (1996 June 30), i.e. 23 days prior to our first observation, and likely with a  $V$  peak magnitude of about  $13.9 \pm 0.3$  ( $B = 13.7 \pm 0.3$ ). In the following, we will adopt this estimate of the  $V$  maximum epoch as reference time. The epoch of the  $B$ -band

**Table 1.** Magnitudes of the local sequence stars as identified in Figure 1.

star	<i>U</i>	<i>B</i>	<i>V</i>	<i>R</i>	<i>I</i>
1	20.36(06)	19.33(03)	18.27(02)	17.60(03)	17.06(03)
2*	15.67(03)	15.84(03)	15.45(02)	15.16(02)	14.89(02)
3	21.26(11)	19.98(04)	18.52(02)	17.58(03)	16.67(03)
4	18.77(04)	18.37(05)	17.58(03)	17.09(03)	16.63(02)
5	20.37(10)	19.18(05)	17.68(03)	16.37(03)	14.89(03)
6**	17.67(05)	17.00(05)	16.11(03)	15.53(04)	15.05(03)
7	15.70(02)	15.61(02)	15.00(02)	14.63(03)	14.31(03)

(\*) For this star we have also IR magnitudes:

$J=14.55(03)$ ,  $H=14.18(03)$ ,  $K=14.28(03)$

(\*\*) Double star: magnitudes refer to the brighter component

peak is coincident with that of the *V* maximum. However, we stress that these estimates are subject to relatively large uncertainty, since the maxima themselves were not observed and Type IIL SNe show a variety of photometric behaviours around the maximum epochs (Faran et al. 2014). In Table 2, the main parameters of the *UBVRI* light curves of SN 1996al are summarised.

An inflection point in the linear decline is observed at about day +150. Between +150 and about +320 days the light curves, though not well sampled, show declines that match the  $^{56}\text{Co}$  decay rate ( $0.98 \text{ mag}(100)^{-1} \text{ days}$  (Table 2). From +320 to +450 days the light curves level-out to a new plateau, where the *V* light curve slightly increases in luminosity by +0.2 mag, and *R* by  $\sim +0.1$  mag. After this plateau, the *BVRIJ* light curves start a monotonic decline (with some modulation in the *R*-band) with rates very similar to those observed between 150 and 300 days (Table 2).

### 2.1.2 Colour curves

In Figure 3, the extinction corrected<sup>3</sup>  $(U - B)_0$ ,  $(B - V)_0$  and  $(V - R)_0$  colour curves of SN 1996al are plotted along with those of two bright SNIIL, SNe 1980K and 1990K, and SN 1998S.

The early  $(U - B)_0$  colour curve of SN 1996al is consistent with that of SN 1980K. It shows a smooth increase reaching a value of  $-0.1$  mag at about 70 days. From day +140, it experiences a linear increase from  $-0.30$  to  $+0.13$  mag at phase 450 days, although the colour curve sampling is poor. However, it never reaches the red colours observed in SN 1980K ( $+0.5$  mag).

The  $(B - V)_0$  colour curve shows an overall similar behaviour as the  $(U - B)_0$  colour curve. It is initially blue ( $+0.07$  mag), then it smoothly increases to a maximum of  $+0.54$  mag at  $\sim 70$  days, followed by a slow decline. At late times, the  $(B - V)_0$  colour curve remains substantially constant at  $+0.34$  mag with a small decrease to about 0.24 mag at about 460 days after maximum.

The overall appearance of the  $(B - V)$  colour curve is very similar to that of SN 1998S, and not very discrepant

from that of SN 1980K, although somehow displaced in phase. Also in this colour, SN 1996al never reaches the red values ( $(B - V) \sim 1$  mag) shown by SN 1980K. SN 1990K, another bright SNIIL studied by Cappellaro et al. (1995), showed very red colours already at maximum. At phases close to  $\sim +160$  days, all four SNe have similar  $(B - V)$  colours. Finally, the SN 1996al  $(V - R)$  colour curve experiences a gradual “reddening” with early values similar to those seen in SN 1990K. After +100 days, the  $V - R$  colour curves of the two SNe show a plateau-like feature, with a  $(V - R) \sim 0.41$  mag for SN 1996al. Starting at about day +120,  $(V - R)$  further increases to  $\sim 0.9$  mag, and remains thereafter almost constant.

## 2.2 Reddening and distance to NGC 7689

The Galactic reddening towards NGC 7689 is  $A_B=0.051$  mag (Schlegel et al. 1998). The higher S/N ratio spectra of SN 1996al show narrow absorptions due to interstellar NaID, suggesting that some light extinction may occur within the parent galaxy. The mean EW of this doublet averaged over 10 measurements is  $0.60 \pm 0.08 \text{ \AA}$ . Using the relation  $E(B - V) \sim 0.16 \times EW(\text{NaID})$  of Turatto et al. (2003) yields  $E(B - V)_{\text{host}} \sim 0.10 \pm 0.05$  mag. In the following, we will adopt for SN 1996al a total reddening of  $E(B - V)_{\text{tot}} = 0.11 \pm 0.05$  mag.

From the NaID interstellar lines we also derive a mean recessional velocity of  $1835 \pm 68 \text{ km s}^{-1}$  for NGC 7689, to be compared with the optical ( $1974 \pm 6 \text{ km s}^{-1}$ ) and radio ( $1970 \pm 5 \text{ km s}^{-1}$ ) velocities given by NED<sup>4</sup>. The difference ( $-135 \text{ km s}^{-1}$ ) is likely due to the host galaxy rotation, projected along the line-of-sight (LOS).

Adopting a value of  $H_0=73 \text{ km s}^{-1} \text{ Mpc}^{-1}$  along with the radio heliocentric radial velocity of  $1967 \text{ km s}^{-1}$ , and correcting it for Local Group infall onto the Virgo cluster, NED gives for NGC 7689 a distance modulus of  $\mu_B = 31.98$  (24.89 Mpc).

On the other hand, using the relative distance of NGC 7689 from the Virgo cluster (of 1.37, Kraan-Korteweg 1986), and assuming a Virgo cluster distance of 15.3 Mpc (Freedman et al. 2001), a distance modulus of  $\mu_B = 31.61$  mag (20.96 Mpc) is derived for NGC 7689.

The mean value of the above estimates,  $\mu_B = 31.80 \pm$

<sup>3</sup> using the Cardelli et al. (1989) extinction law, and the reddening value discussed in Sect. 2.2

<sup>4</sup> <http://ned.ipac.caltech.edu>

**Table 2.** *UBVRIJ* light curve parameters.

band	post-max	start short	plateau	plateau	post-plateau	decline	decline
	decline	plateau	duration	mag	decline	(150–300 days)	(> 450 days)
	$\text{mag}(100\text{days})^{-1}$	days	days	mag	$\text{mag}(100\text{days})^{-1}$	$\text{mag}(100\text{days})^{-1}$	$\text{mag}(100\text{days})^{-1}$
<i>U</i>	10.73	+30	2	15.01	4.98	$\geq 0.84$	
<i>B</i>	7.46	+30	2	15.35	4.85	0.85	0.84
<i>V</i>	5.55*	+34	7	15.28	4.65	0.89	0.86
<i>R</i>	5.03	+34	7	14.95	4.38	0.67	0.67
<i>I</i>	5.12	+34	7	14.83	4.31	0.95	0.98
<i>J</i>							1.24

(\*) excluding the visual estimation of Evans et al. (1996)

0.20 mag (22.91 Mpc) is adopted throughout the paper as distance modulus for NGC 7689.

### 2.3 Absolute magnitudes and bolometric light curve

With the above assumptions for extinction and distance (using the Cardelli et al. (1989) extinction law), we obtain  $M_B \sim -18.6 \pm 0.4$  and  $M_V \sim -18.2 \pm 0.3$  for the SN absolute *B* and *V* magnitudes at maximum. These are similar to those of the “bright” SNIIL sub-class (which have a  $\langle M_B \rangle = -19.0 \pm 0.6$  mag, rescaled to  $H_0=73$  km s<sup>-1</sup> Mpc<sup>-1</sup>; Patat et al. 1994).

In order to compute the energy budget of SN 1996al and to simplify the comparison with theory, it is useful to determine the bolometric light curve. Unfortunately, no observations at UV, X-ray or radio wavelengths are available. We are then limited to derive a pseudo-bolometric (*UBVRIJHK*, or *uvoir*) light curve. This was obtained first adding the *UBVRIJ* contributions and then calculating the *HK* contributions in the phase range 153–408 days, assuming during this period a constant  $H - K$  colour. The *HK* contribution resulted in  $\log L_{UtoK} - \log L_{UtoJ} = 0.08 \pm 0.01$  dex for this period. We made the assumption that the IR contribution to the total luminosity remained constant at earlier epochs. The bolometric curve shown in Figure 4 shares all relevant features already noted in chromatic curves: the overall linear decay up to 150 days after explosion, including a hint of a plateau around day +30. It shows a break in the decay at around day +150, then a <sup>56</sup>Co like decay up to about day +300. This is followed by a plateau-like phase with an almost constant bolometric luminosity (+300 to +450 days) and, finally, a new decay with a rate close to that of <sup>56</sup>Co.

In Sect. 3, we will argue that most probably in SN 1996al, the CSM/ejecta interaction is the primary energy source for a large part of its evolution. However, comparing the early part of the linear tail of SN 1996al, between  $\sim 150$  and 300 days after explosion, with the radioactive tail of SN 1987A, one can derive an upper limit for the <sup>56</sup>Ni ejected in the explosion. Assuming a <sup>56</sup>Ni mass of  $0.075 \pm 0.005 M_\odot$  for SN 1987A (Danziger 1988; Woosley, Hartmann, & Pinto 1989), and adopting for SN 1996al a scaling factor of 0.24 as suggested by Figure 4, we derive that the <sup>56</sup>Ni ejected in the explosion of SN 1996al is  $\lesssim 0.018 \pm 0.007$

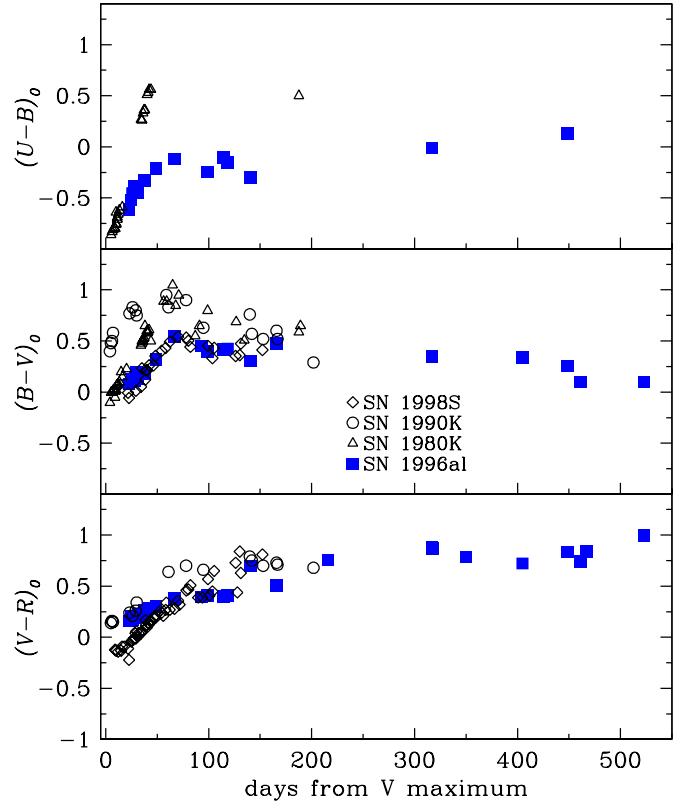


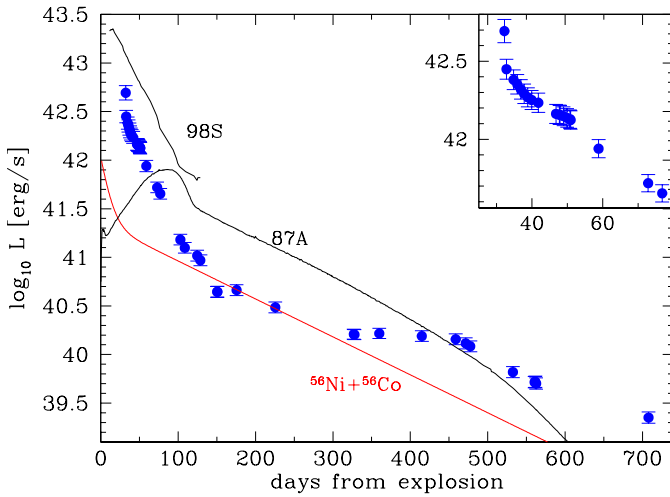
**Figure 3.** The de-reddened colour curves of SN 1996al are compared with those of SN 1980K and SN 1990K (Cappellaro et al. 1995).

$M_\odot$ , where the error budget is equally dominated by the uncertainties on the SN 1996al distance, the epoch of the explosion, and the SN 1987A <sup>56</sup>Ni mass. We can also estimate the <sup>56</sup>Ni mass from the observed luminosity assuming full  $\gamma$ -rays trapping and a rise time to maximum of 10 days. Hence, the amount of <sup>56</sup>Co necessary to fit the tail from 100 to 300 days is  $\lesssim 0.017 \pm 0.003 M_\odot$ , fully consistent with that derived from the SN 1987A scaling.

**Table 3.** Main parameter values for SN 1996al and its host galaxy.

Parent galaxy	NGC 7689
Galaxy type	SABc †
Recession velocity	1970 km s <sup>-1</sup> †
Distance modulus ( $H_0 = 73 \text{ km s}^{-1} \text{ Mpc}^{-1}$ )	$31.80 \pm 0.2 \text{ mag}$
$E(B - V)$	$0.11 \pm 0.05 \text{ mag}$
$RA_{SN}$ (J2000.0)	$23^h 33^m 16^s .29 \pm 0.03$
$Dec_{SN}$ (J2000.0)	$-54^\circ 04' 59" .69 \pm 0.05$
Offset from galaxy nucleus	30" N
Date of $B, V$ maxima (MJD)	$50265 \pm 2.0$ (Jun. 30, 1996)
Magnitude at max	$B = 13.7 \pm 0.3, V = 13.9 \pm 0.3 \text{ mag},$
$\beta_{100}^B$	4.84 mag

† from NED

**Figure 4.** Bolometric *uvoir* light curve of SN 1996al. A zoom of the *uvoir* curve in phases near maximum is shown in the upper-right box. For comparison, the  $^{56}\text{Ni}+^{56}\text{Co}$  decay model in the hypothesis of full  $\gamma$ -rays trapping is also reported. The rise time to maximum was assumed to be 10 days.

A summary of the main parameter values inferred for SN 1996al and its host galaxy is provided in Tab. 3.

## 2.4 Spectroscopy

Spectroscopic observations spanned from days +23 to +5542, with an excellent temporal coverage during the first two months. Table A2 lists the date (col. 1), the Modified Julian Day (col. 2), the phase relative to  $t_{V,max}$  (col. 3), the wavelength range (col. 4), the instrument used (col. 5), and the resolution as measured from the FWHM of the night-sky lines (col. 6). At some epochs, almost contemporary spectra were obtained. These were merged to produce higher S/N spectra or wider wavelength ranges.

The spectra were reduced following standard MIDAS and IRAF routines. The XShooter (Vernet et al. 2011) spectra were reduced using the ESO-XShooter pipeline version 1.1.0. One dimensional spectra were extracted weighting the signal by the variance based on the data values and a poisson/CCD model using the gain and readout-noise param-

eters. The background to either side of the SN signal was fitted with a low-order polynomial, and then subtracted. The flux calibration and telluric absorptions modelling were achieved using spectra of spectrophotometric standard stars. Most spectra were taken through a slit aligned along the parallactic angle, or normalised to spectra taken with a wider ( $\geq 5$  arcsec) slit. The flux calibration of the spectra was checked against photometry (using the IRAF task STSDAS.HST\_CALIB.SYNPHOT.CALPHOT) and, if discrepancies occurred, the spectral fluxes were scaled to match the photometry. On nights with fair sky transparency, the agreement with photometry was within 15%. The spectra of SN 1996al are shown in Figure 5.

### 2.4.1 A brief description of the overall spectroscopic evolution

The earliest spectra show a relatively blue continuum ( $T_{bb} \sim 12000 \text{ K}$ ), once corrected for reddening and redshift. The continuum becomes progressively redder with phase, reaching a temperature of about  $6500 - 7000 \text{ K}$  at phases later than  $\sim 60$  days (see also Sect. 3.4). Early spectra are dominated by broad  $H\alpha$  and  $H\beta$ , and the blend of  $\text{He I } 5876\text{\AA}$ - $\text{Na I D}$  lines.

The Balmer lines show complex profiles (see Figures 6 and 7), and the decomposition of the early  $H\alpha$  profile is detailed in Figure 8a.  $H\beta$  has a very similar profile. The detailed evolution of the Balmer lines (in particular  $H\alpha$ ) is discussed in Sect. 3.2.

Another intense, broad emission detected in our first spectrum is a blend of the  $\text{He I } 5876\text{\AA}$ - $\text{Na I D}$  lines. It has a FWHM of  $\sim 260 \text{ \AA}$  centered at  $\sim 5906 \text{ \AA}$ , though it shows a double-peaked profile (see Figure 6). The detailed evolution of this and other unblended He lines will be discussed in Sect. 3.3.

A broad absorption is observed with a minimum at  $5079 \text{ \AA}$ . Assuming it is  $\text{Fe II } 5169 \text{ \AA}$ , it gives an expansion velocity of  $\sim 5200 \text{ km s}^{-1}$ . Also, our early spectra show narrow Fe II ( $5018\text{-}5169 \text{ \AA}$ ) lines with P-Cygni profiles. These are clearly visible in the SN spectra up to phase +43 days, with a mean velocity from the absorption minima of  $480 \pm 150 \text{ km s}^{-1}$ .

The narrow lines likely arise from a dense CSM, which was ionised either by the X-UV flash shock break-out, or by the UV photons emitted by the progenitor star (as suggested by the  $H\alpha$  emission seen around the progenitor before the explosion, cf. Sect 3.1). The CSM, which is recombining at

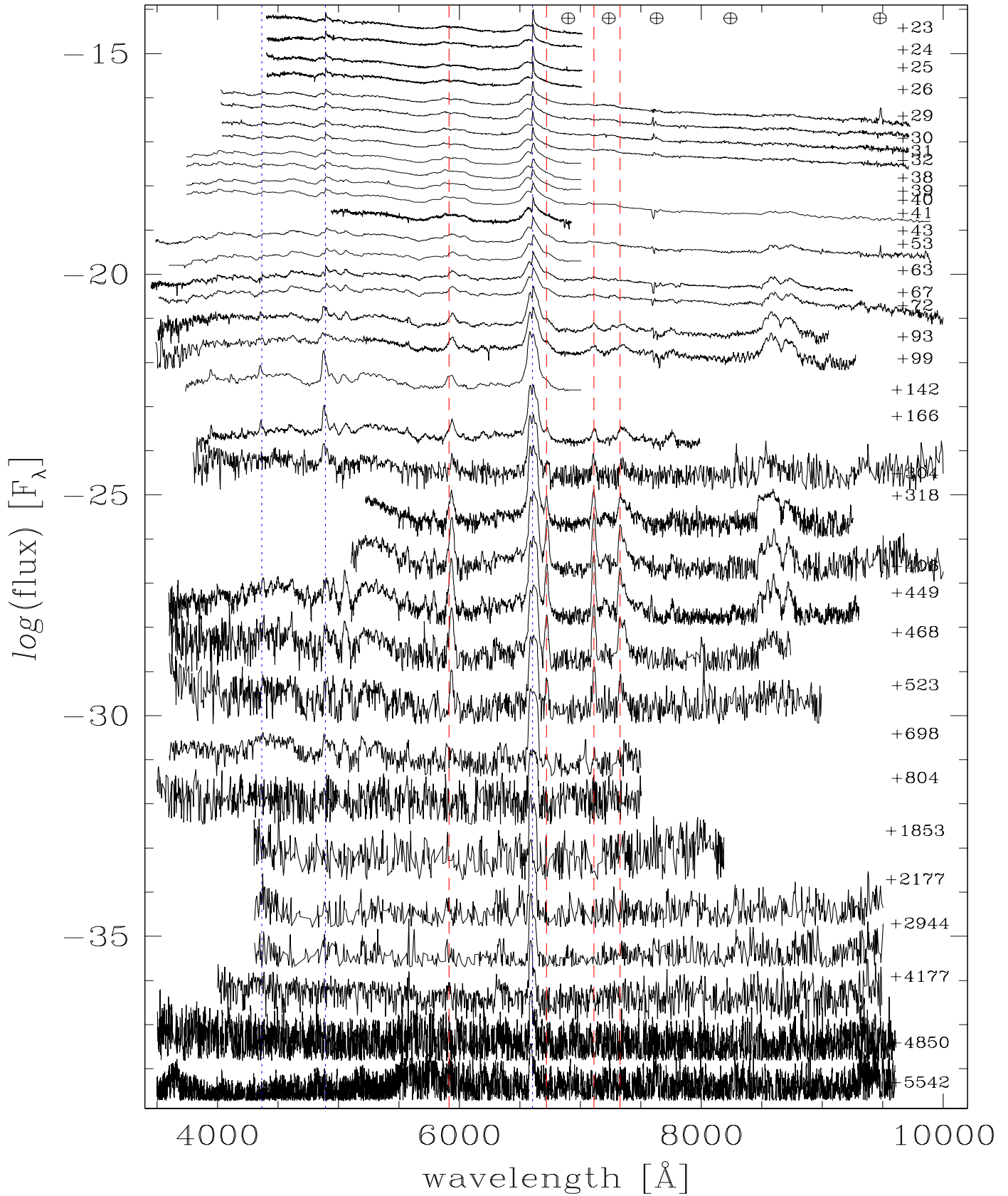


**Figure 5.** Spectral evolution of SN 1996al. Wavelengths are in the observer's frame. The ordinate flux scale is optimised to the first spectrum, and all others are arbitrarily shifted downwards. In a few cases, noise spikes have been manually removed. From blue to red wavelengths, the dotted (blue) vertical lines mark the positions of H $\gamma$ , H $\beta$ , and H $\alpha$ , respectively; while the dashed (red) lines mark the 5876  $\text{\AA}$ , 6678  $\text{\AA}$ , 7065  $\text{\AA}$  and 7281  $\text{\AA}$  He I transitions. The positions of the most intense telluric absorption bands are marked.

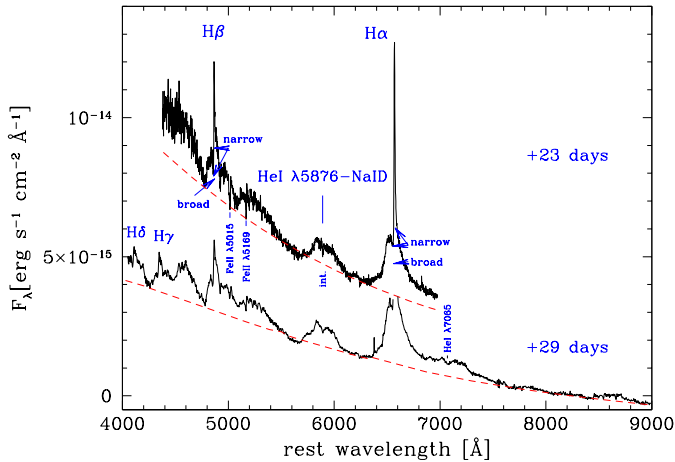


**Figure 6.** Earliest spectra of SN 1996al corrected for redshift and reddening. The main features are identified, together with the different components seen in  $H\beta$  and  $H\alpha$ . The narrow absorption (marked "int.") on the top of the He I  $\lambda 5876$ -Na ID emission is due to Na ID Galactic absorption. The dashed (red) lines are blackbody fits of the spectral continuum ( $T=10100^{\circ}\text{K}$  and  $8600^{\circ}\text{K}$  for +23 and +29 days, respectively; see Sect. 3.4).

these phases, has a bulk velocity of  $\sim 250 \text{ km s}^{-1}$ , as deduced from  $H\beta$  narrow emission, but extends up to  $\sim 2000 \text{ km s}^{-1}$ , as inferred from the blue edge of the narrow Balmer absorptions.

The spectrum does not change significantly during the first few weeks, with the continuum becoming progressively redder. At phase +29 days, we are able to monitor for the first time a more extended wavelength range (see Figure 6). Starting from the blue-end of the spectrum, we see  $H\delta$  and  $H\gamma$ . They have complex profiles similar to those of  $H\beta$  and  $H\alpha$ . Redward to  $H\alpha$ , there is possible evidence for the He I  $7065 \text{ \AA}$  transition (see discussion in Sect. 3.3), while the He I  $6678 \text{ \AA}$  might be embedded in the  $H\alpha$  red wing. The +41 day spectrum shows broad emissions (centered at  $8531$  and  $8677 \text{ \AA}$ ) due to the Ca II IR triplet. The FWHM of the total emission is about  $3500 \text{ km s}^{-1}$ . The He I  $5876 \text{ \AA}$ -Na ID feature still has a very broad profile similar to the emission red-ward of  $H\alpha$ , which we interpret as mostly due to He I  $7065 \text{ \AA}$ .

The subsequent spectrum (phase +53 days) shows the appearance of other important features. The broad  $H\alpha$  profile is now better reproduced with a Gaussian profile (having a  $\text{FWHM} \sim 5700 \text{ km s}^{-1}$ , see Table A3), and its red wing is better fitted adding a broad ( $\text{FWHM} \sim 4500 \text{ km s}^{-1}$ ) emission centered at  $6699 \text{ \AA}$  (rest frame) in Figure 8b. We identify this emission as the He I  $6678 \text{ \AA}$  transition.

In general, the He I lines become more symmetric and narrow with time, with their flux sharply rising after +300 day (cfr. Sect. 3.3). The He I transitions show peculiar line ratios (see Figure 5 and Tables A3, A4) and then disappear at about phase +700 days (see Sect. 3.3 for a detailed discussion on the He I lines evolution).

As at these early epochs the FWHM velocities of the  $H\alpha$  broad component are similar to those of the He I lines, it is plausible that these lines originate in the same region

of the ejecta and are probably powered by the same mechanism.

The evolution of the  $H\alpha/H\beta$  ratio tells that this mechanism is not photoionisation. In fact, starting from phase +43 days this ratio starts a linear increase from a value close to the case B recombination value of 2.8, to  $\sim 10 - 12$  about 1000 days after the  $V$ -band maximum (see Sect. 3.2).

At epochs  $\geq +142$  days, the Balmer lines undergo another profound change in their profiles (see Figure 8c). The narrow lines arising in the un-shocked CSM are not visible anymore. This could either imply that the ejecta have overtaken the bulk of the denser CSM or, more likely, that the CSM has by that time completely recombined. The  $H\alpha$  profile is now well fitted with three Lorentzians of comparable FWHM centered at  $6539 \text{ \AA}$ ,  $6569 \text{ \AA}$  and  $6597 \text{ \AA}$  (see Table A4 and Sect. 3.2). These components will be visible along the residual SN lifetime. We will refer to them as Blue, Core and Red components. With time, the Core and Red components become weaker and weaker in comparison with the Blue one (see Figure 7).

As already stressed,  $H\beta$  becomes weaker with time with respect to  $H\alpha$  (see Sect. 3.2), and the  $H\alpha/H\beta$  ratio reaches values exceeding about 15 at the latest epochs.

### 3 DISCUSSION

#### 3.1 The progenitor star

A search for archival material concerning the parent galaxy of SN 1996al returned a deep  $H\alpha$  image performed for a portion of NGC 7689 with the Rutgers Imaging Fabry-Perot instrument + CCD Camera attached at the Cassgrain focus of the CTIO 4-m Blanco telescope. The image was taken in the context of a work aimed at studying the star formation in the disk of a sample of Sa galaxies (Caldwell et al. 1991). Luckily enough, the portion of NGC 7689 imaged on September 1988 included the zone where SN 1996al appeared eight years later. Unfortunately, these were the first digital observations performed with modern CCDs and at that time CTIO was not yet equipped with a digital archive (CTIO director, private communication). For this reason, the original frames stored on a 9-track tape by the observer were lost. In order to properly place the SN location on the map we digitalised Plate 29 of Caldwell et al. and aligned it with the VLT+FORSS2  $H\alpha$  frame obtained under good seeing conditions on 2002, June 16 (see caption of Figure 1). After the alignment, performed with about 40 sources around the SN positions, we found that a faint  $H\alpha$  region is coincident with the SN position, within an uncertainty of  $\pm 0.75''$ . Given the relatively clean environment at that position (cfr. Figure 1), we believe that the  $H\alpha$  emission visible in the Caldwell et al. image was indeed associated with the progenitor star of SN 1996al.

The  $H\alpha$  luminosity of this source measured by Caldwell et al. but not reported in their original paper, given the distance and reddening assumed in this work (see Table 3), is  $\log L_{H\alpha} \sim 37.28 \pm 0.10$  dex. For consistency, we checked the Caldwell et al.  $H\alpha$  measurements of few H II regions close to the SN 1996al position with those derived from the FORSS2  $H\alpha$  frame, and found a very good agreement.

The  $H\alpha$  pre-explosion luminosity is compared with those



of some possible progenitor systems for SN 1996al in Table 4. The comparison indicates that the  $H\alpha$  emission coming from the SN 1996al progenitor is similar to that expected from hot LBV stars, and lower than that measured in SN-impactor/LBVs prior to a major outburst. This is consistent with the finding of Kennicutt & Hodge (1980), that H II regions in NGC 628 with  $\log L_{H\alpha} < 37.90$  dex have a radius  $< 200$  pc, and are supported by the radiation field of a star with a spectral type later than O4 Ia.

After profile decomposition (see Figure 8 and Table A3), the narrow  $H\alpha$  component visible in the first SN spectrum has a flux of  $\sim 9 \times 10^{-14}$  erg s $^{-1}$  cm $^{-2}$ , which provides a line luminosity of  $\log L \sim 39.85$  dex. This is more than two dex higher than the pre-explosion  $H\alpha$  luminosity (see Table 4). The abrupt increase of the narrow  $H\alpha$  luminosity is a clear indication that the SN shock-break out or ejecta/CSM interaction ionised a much larger fraction of CSM around the progenitor star than the SN progenitor alone.

### 3.2 The evolution of the Balmer lines

The profile of Balmer lines, in particular  $H\alpha$ , shows a multi-component, complex evolution which allows us to track the restless mass loss activity of the progenitor star. It also indicates an asymmetric distribution of the emitting gas. In the following, we will have a close look into the  $H\alpha$  evolution in four temporal intervals.

#### Days +23 to +43

The  $H\alpha$  profile consists of a broad Lorentzian emission with, super-posed, a narrow P-Cygni like component. The  $H\alpha$  profile does not change (see Figure 7) until phase  $\lesssim +40$  days, which coincides with the end of the "short plateau" (see Figure 2).

At the same time, the expansion velocity obtained from the  $H\alpha$  FWHM of the broad component decreases from  $\sim 6500$  km s $^{-1}$  to  $\sim 5600$  km s $^{-1}$ , while the maximum velocity deduced from the  $H\alpha$  blue wing remains constant at about 12000 km s $^{-1}$  (see Table A3 and Figure 9). The average wind velocity as given by the width of the narrow emission shows some scatter around the value of  $\sim 440$  km s $^{-1}$ . The mean FWHM of the narrow absorption is about 890 km s $^{-1}$  (see Table A3 and Figure 9).

The  $H\alpha$  luminosity evolution is negligible (see Figure 10), and the  $H\alpha/H\beta$  flux ratio, which remains constant at about 2.68 (see Figure 11), is close to case B recombination (Osterbrock 1989).

#### Days +53 to +101

The broad  $H\alpha$  is now best fitted by a Gaussian profile with a FWHM decreasing from 5700 km s $^{-1}$  to 3250 km s $^{-1}$ , though faint, extended wings are still visible (see Figure 8b). The maximum velocity deduced from the  $H\alpha$  blue wing remains, instead, constant at about 10500 km s $^{-1}$  (see Table A3 and Figure 9).

Again, these velocities are similar to those of the He I lines, hence we suppose that the lines originate in the same region of the ejecta. Since in the next Section we will demonstrate that at these phases the He I lines are powered by ejecta-CSM interaction, we believe that the same mechanism also supports the  $H\alpha$  flux. At day +100, the  $H\alpha$  luminosity is about 0.3 dex lower than the  $H\alpha$  luminosity for the twin

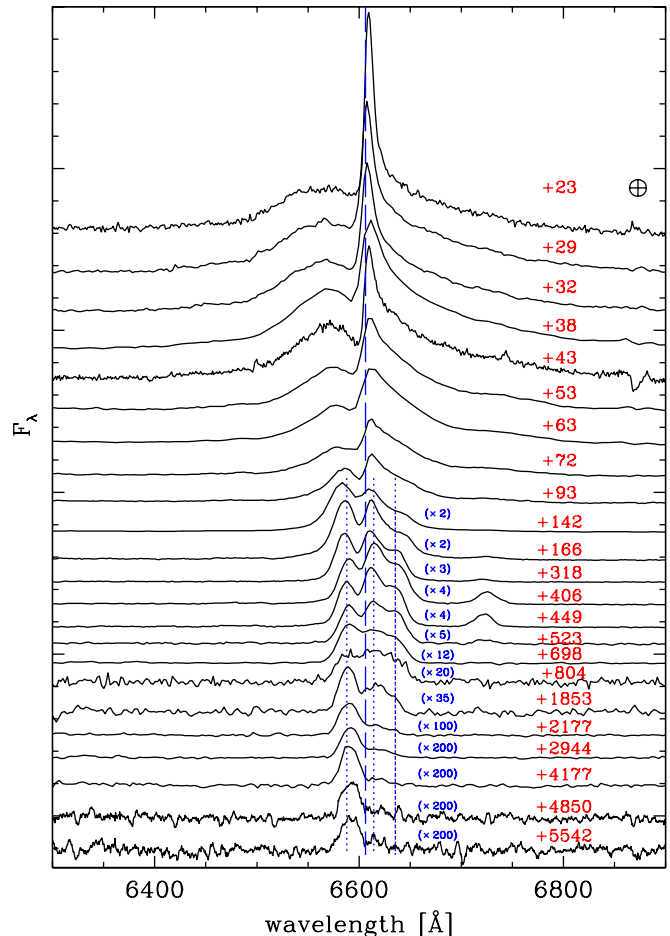


**Figure 7.**  $H\alpha$  profile evolution of SN 1996al. Wavelengths are in the observer's frame. The feature near 6875 Å in the +43 days spectrum is a residual from an poorly removed telluric band.

SN 1994aj at the same phase (Paper I), but is very similar to that of SN 1996L (Paper II).

The velocity of the wind, as derived from both the narrow emission and absorption features, shows a mean value of  $\sim 590$  km s $^{-1}$ .

In this period, the  $H\alpha/H\beta$  flux ratio begins to increase, reaching a value of  $\sim 6.5$  at a phase of +100 days. This could be a clue that  $H\alpha$  becomes more collisionally excited (Branch et al. 1981), in line with the proposed scenario (see Sect. 3.5).

#### Days +142 to $\sim +800$

From day +142, the  $H\alpha$  profile undergoes another profound change. The  $H\alpha$  profile is now better fitted by three Lorentzian components (see Figure 8c), up to phase +523 days, and later on with three Gaussian components. They are centered at  $\sim -1100$  km s $^{-1}$  (the Blue component), 270 km s $^{-1}$  (the Core component) and +1550 km s $^{-1}$  (the Red component) with respect to the nominal position of  $H\alpha$ . The three narrower components are visible along the remaining life of the SN and their wavelengths do not change significantly with time (see Figures 7 and 12).

Since their earliest appearance, these components show a very similar FWHM, the Red component being the broadest (FWHM $\sim 970$  km s $^{-1}$ ), followed by the Core component (FWHM $\sim 950$  km s $^{-1}$ ), while the Blue component has a FWHM $\sim 850$  km s $^{-1}$  (see Table A4 and Figure 9).

Between 142 and 800 days, the flux ratios of the different components stay constant, with the Core and Blue components carrying the largest fraction of the H $\alpha$  flux (30-40% each). In this lapse of time, the H $\alpha$  luminosity shows a relatively flat and linear (in a log-log diagram) decrease up to phase  $\sim +500$  days, followed by a sharper drop (by almost 1 dex) up to about +800 days. This behaviour resembles that of the bolometric curve which, however, stops at about 700 days after explosion (see Figure 4).

We interpret these H $\alpha$  components as the result of the interaction between a mostly spherical ejecta with an highly asymmetric CSM. The geometric configuration of the system will be discussed with more detail in Sect. 3.5. The H $\alpha$ /H $\beta$  flux ratio continues to steadily rise (see Figure 11) to a value of about 10.

#### Later than +800 days

There is an observational gap between +800 and +1850 days. From day +1853 the H $\alpha$  profile is again fitted by the three Gaussians mentioned before, and both the H $\alpha$  flux and the bolometric curve show steeper evolutions.

While the overall flux carried out by the line dim by 0.28 dex during this time interval, the relative intensities of the three components change: the Blue component is now much stronger with respect to the other two, while the Red one remains the dimmest (see Figure 13). At phase +2177 days, the flux ratio of the Core component decreases to the level of the Red component one, while the Blue component is carrying almost 80% of the line flux. After this phase, the line ratios do not change very much. The sharp change in the relative flux ratios may be a signature of either a sudden dust formation in the SN ejecta, or a progressive quenching of the interaction between the ejecta and the receding part of the CSM. Most probably, as the central wavelengths of the Core and Red emission peaks do not show any evolution (see Figure 12), both scenarios are at work. Also the Blue component does not show any shift from the central position. For this reason, if dust is forming, it condensates in the inner part of the ejecta or in the clumps where the Core and Red H $\alpha$  components originate.

Starting from  $\sim 2900$  days after the explosion, the H $\alpha$  luminosity (see Figure 10) decreases below the luminosity emitted by the precursor star. This, along with its distorted profile, proves that most of the H $\alpha$  flux comes from the SN itself and that the ambient contamination is by now negligible. Moreover, this is a clue that the H $\alpha$  source detected before the explosion was indeed associated to the precursor star and that it has been swept up by the SN ejecta.

### 3.3 The He I lines

In our first spectra, the best evidence for the presence of helium is the broad, asymmetric bump (FWHM $\sim 11000$  km s $^{-1}$ ) centered at about 7065 Å (rest frame) that can be identified as He I 7065 Å (see Figure 6). Figures 14 and 15 show the complete evolution of He I 7065Å, the only

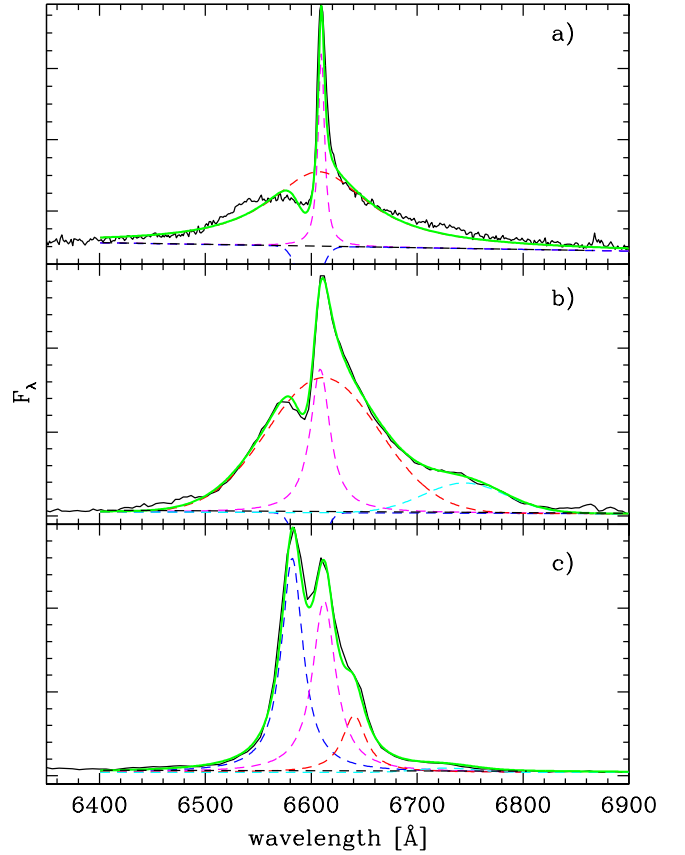


**Figure 8.** Deconvolution of the H $\alpha$  profile of SN 1996al at phases +23 days (a); +53 days (b) and +142 days (c), key epochs which attest the profound modification of the line profile. Wavelengths are in the observer’s frame. In panels (a) and (b) the H $\alpha$  line profile has been fitted with a broad emission (Lorentzian in the first, Gaussian in the second; *dashed*, red line), a narrow Lorentzian emission component (*dashed*, magenta line) and a narrow Gaussian absorption component (*dashed*, blue line; cut down for display purpose). The feature red-ward of H $\alpha$  in the +53 days spectrum (Gaussian; *dashed*, cyan line) is He I 6678Å. In panel (c) the H $\alpha$  profile has been fitted with three Lorentzians: the Blue (*dashed*, blue line), the Core (*dashed*, magenta line) and the Red component, respectively. The He I 6678Å line (Gaussian; *dashed*, cyan line) is also present, although now much fainter (see Sect. 3.3).

helium transition which is not contaminated by close-by strong lines. In fact, this is not the case for He I 5876 Å, which could be heavily contaminated by the nearby Na I D doublet. An estimate of the relative contribution of two lines throughout the complete spectroscopic evolution of SN 1996al is a very difficult task. The last phase in which the He I lines are unequivocally detected is +523 day (see Figure 5).

In Figure 16, we compare the profiles of He I 5876 Å - Na I D with the He I 7065 Å line, during the first 100 days of the SN evolution. In the first two spectra (+29 and +32 days) they are very similar, both in the overall profile and

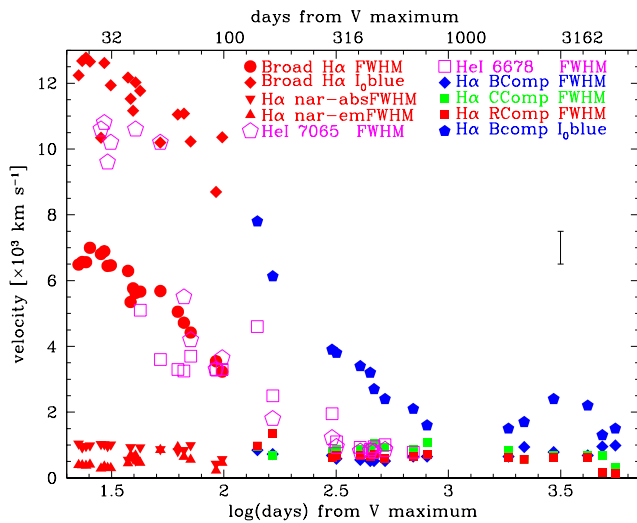


**Figure 9.** Velocity evolution of the H $\alpha$  components and the He I 6678-7065Å transitions. The mean error bar ( $\pm 500 \text{ km s}^{-1}$ ) for the broader lines is shown. For the narrowest features (those with  $\text{FWHM} \lesssim 2000 \text{ km s}^{-1}$ ), the error bar is smaller than the symbol.

velocity limits. The lines show a double peaked profile with the blue one peaking at  $\sim -2000 \text{ km s}^{-1}$  and the red one at  $\sim 3500 \text{ km s}^{-1}$ , with the red wing extending far to higher velocities ( $\sim 9000 \text{ km s}^{-1}$ ) than the blue one. Thanks to the similarity of the profiles, we may safely conclude that at phases +29, and +32 days the He I 5876 Å - NaID feature is almost entirely due to He. Figure 16 shows that, at least during the first month, the broad wings of the H $\alpha$  profiles are similar to those of He I lines, suggesting that the three lines form in the same, asymmetric region.

Figure 14 also shows that the profile of the He I 7065 Å emission remains unchanged up to +53 days after the V maximum, with the blue bump dominating the line profile. By this time, the profile of He I 5876 Å - NaID feature starts to deviate from that of He I 7065 Å (see Figure 16) with a broad bump emerging slightly redder than the NaID rest wavelength position. Apart from this difference, the two He I lines and the broad H $\alpha$  still share the same basic characteristics (see third panel from top in Figure 16).

Starting from phase +67 days, the He I 7065 Å line shows a new component centered at the rest position, with the blue and red bumps still being visible. Also the He I 5876 Å - NaID feature has an overall similar profile, with an increasingly contribution from the NaID.

Afterwards, (on day +93 and +99) the He I 7065 and 7281 Å features become progressively more symmetric, are centered at the rest position and reach terminal velocities of about  $2500\text{-}3000 \text{ km s}^{-1}$  (see bottom spectra in Figure 14). The He I 5876 Å - NaID profile is different, indicating an increased contribution by NaID (see below). On the contrary, the terminal velocities of the H $\alpha$  broad component are higher, implying different zones of formation. The broad H $\alpha$  component is still coming from the outer, fast-moving region of the ejecta whose emissivity strongly depends on CSM interaction, while the He-NaID lines mostly form in the slow expanding, spherically symmetric inner ejecta. In order to explain the broad He I line profiles at early times, we may conceive two possible alternatives: either some  $^{56}\text{Ni}$

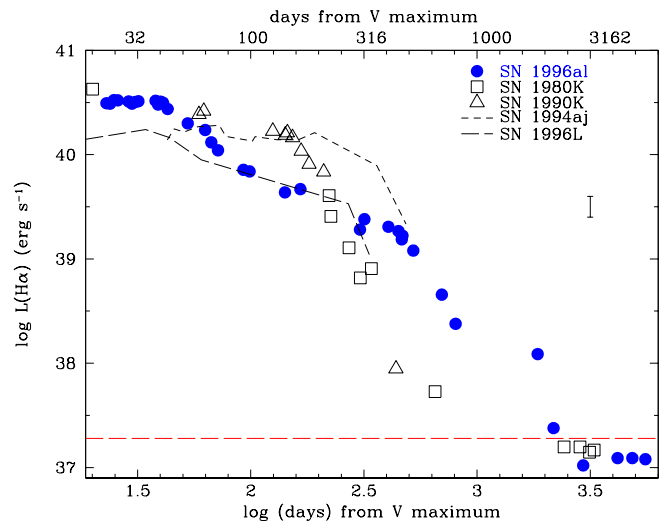


**Figure 10.** H $\alpha$  luminosity evolution of SN 1996al compared with those of SNe 1980K (Uomoto & Kirshner 1986), 1990K (Cappellaro et al. 1995), and the twin SNe 1994aj (Paper I) and 1996L (Paper II). The mean error for the  $\log(L_{\text{H}\alpha})$  of  $\pm 0.10$  dex is reported. The horizontal *long-dashed* (red) line marks the H $\alpha$  flux emitted by the precursor star. The H $\alpha$  luminosities here reported are the total H $\alpha$  flux measurements, which may be slightly different from the sum of the fitting components reported in Tables A3 and A4 and resulting from the deconvolution of the entire line profile. The H $\alpha$  luminosity on day +4178 is the average between the flux measured from the FORS2 spectrum and that derived from the calibrated H $\alpha$  image.

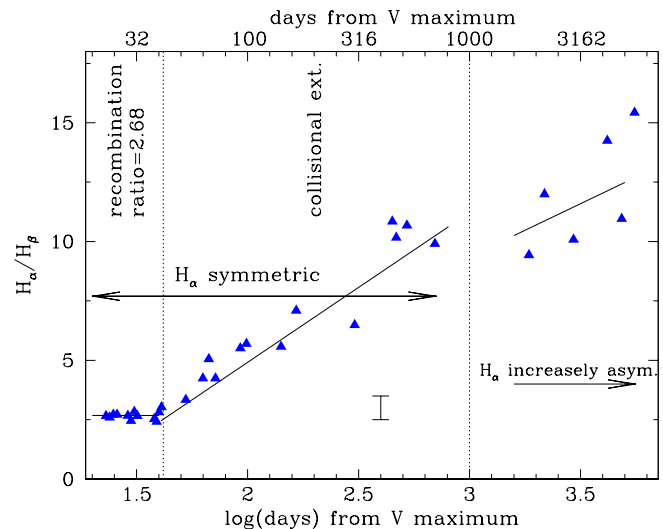


**Figure 11.** Evolution of the H $\alpha$ /H $\beta$  ratio for SN 1996al. The changes of the main properties of H $\alpha$  are labelled. The latest points, after 1000 days, are essentially lower limits since (at these late phases) H $\beta$  barely detectable. The mean error bar for the H $\alpha$ /H $\beta$  ratio ( $\pm 0.5$ ) is shown.

was ejected at high velocity ( $\sim 10000 \text{ km s}^{-1}$ ), or the He I lines were supported by the interaction of the fast expanding symmetric ejecta with an asymmetric CSM. Since starting from about 2 months past explosion the He I lines become symmetric (the inner geometry of the innermost layers ap-

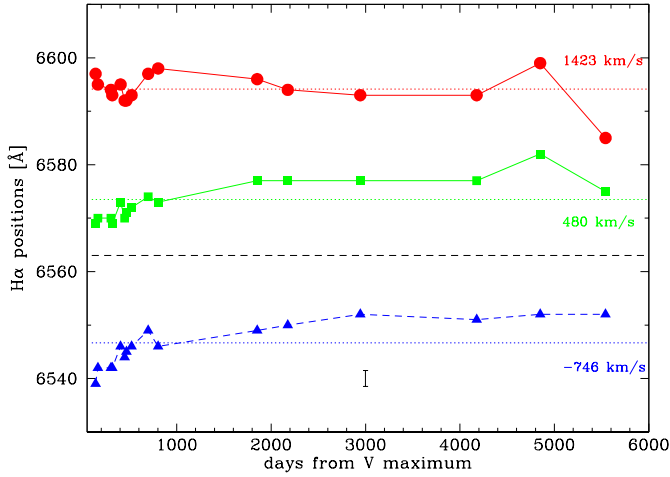


**Figure 12.** Evolution of the positions of the three H $\alpha$  components in the spectra of SN 1996al obtained after day  $\sim 100$ . The mean error bar for the component positions ( $\pm 1.5$  Å) is shown.

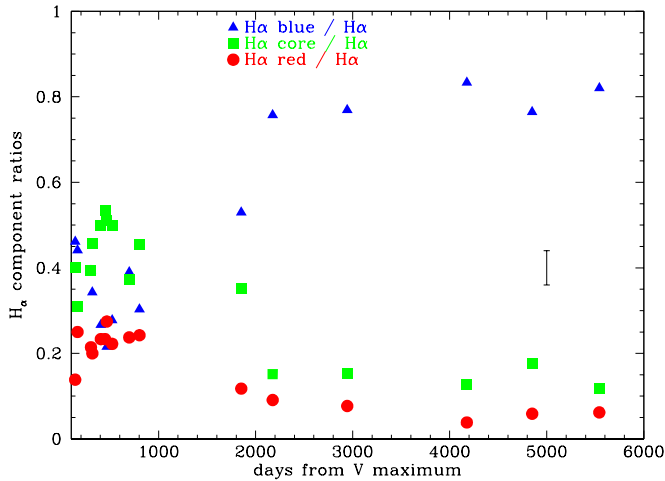


**Figure 13.** Evolution after day  $\sim 100$  of the flux ratios of the three H $\alpha$  components in the spectra of SN 1996al. The flux of each component is divided by the total flux. The mean error bar for the flux ratios ( $\pm 0.08$ ) is shown.

pears to be symmetric), we believe that the interaction scenario is the most likely.

The disappearance of the He I 5876 Å emission line after about day +100 is *prima facie* at odds with the presence of the pronounced He I 7065 Å emission. The clue can be found in the coeval emergence of the NaID emission. In fact, in a co-moving frame the He I 5876 Å photon emitted by the SN ejecta can be redshifted and scattered into the NaID. As a result we see the NaID feature instead of the He I 5876 Å emission. The mechanism can be explored through a model based on a Monte-Carlo simulation (Figure 17). The underlying model assumes freely expanding spherical ejecta with the He I 5876 Å emissivity distribution recovered from the He I 7065 Å profile (Figure 17, inset). The adopted He I 5876 Å flux is 1.2 times larger than that of He I 7065 Å, corre-

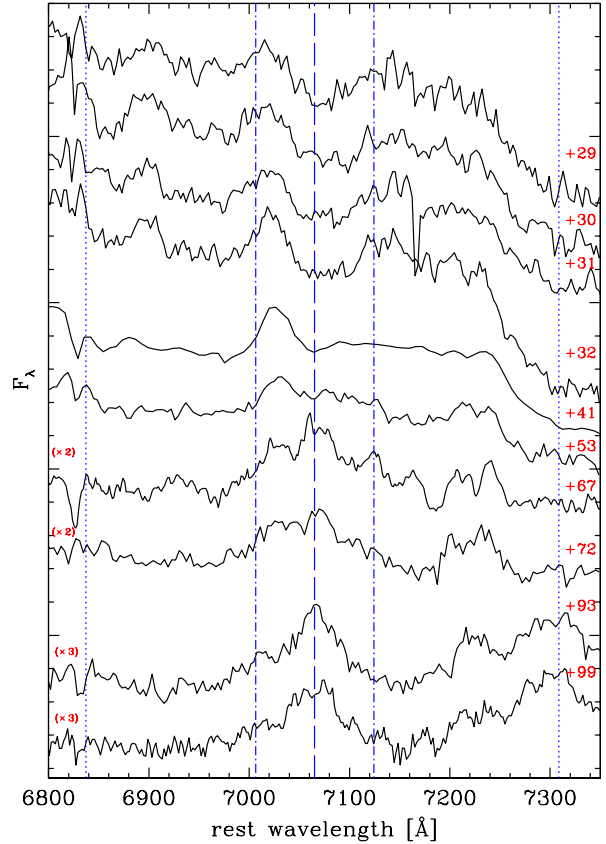


**Figure 14.** Evolution of the He I 7065 Å line profile during the first 100 days. The *dashed* line marks the He I-7065 Å rest frame position, while the *dotted* and *dash-dotted* lines show the expansion velocities of  $\pm 10000$  km s $^{-1}$  and  $\pm 2500$  km s $^{-1}$ , respectively.

sponding to the case of collisional excitation dominating over recombination (Almog & Netzer 1989). The optical depth of the NaID is assumed to linearly fall with increasing velocity from  $\tau(5890) = 20$  at the SN center ( $v = 0$ ), to zero at  $v = 1800$  km s $^{-1}$ . The relative fractions of the Rayleigh and spherical scattering are determined by the Hamilton parameter  $E_1$  which, in the representation of Chandrasekhar (1960), is 1/2 for Na I 5890 Å and zero for Na I 5896 Å. In the optically thin limit, therefore, the scattering phase function for Na I 5896 Å line is spherical, while for Na I 5890 Å line the phase function is the superposition of the spherical (1/3) and Rayleigh scattering (2/3). The latter is taken into account for optical depth  $\tau(5890) \leq 1$ . For  $\tau(5890) > 1$ , the scattering is assumed to be spherical. This approximately accounts for the scattering spherization during the multiple local scattering. It is reassuring that the simulated spectrum (Figure 17) from this simple model provides an excellent fit to the observed emission line.

The evidence of the non-local scattering of He I 5876 Å photons into NaID implies that the late time He I line originates in the inner layers of the SN ejecta.

Figure 15 shows the evolution of the He 7065 Å emission up to almost two years after explosion. While the flux evolution of the line shows a bump between +300 and +500

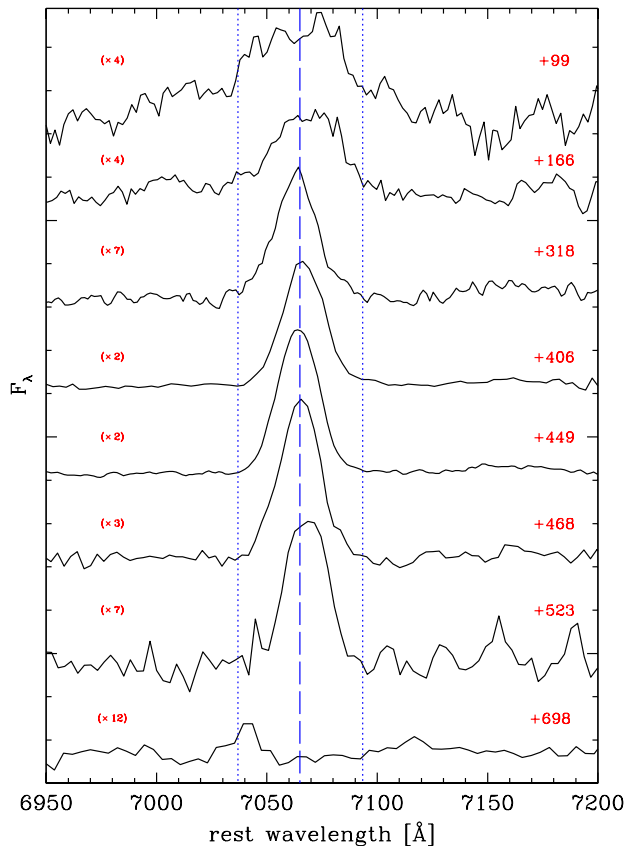


**Figure 15.** Evolution of the He I 7065 Å line profile after 100 days. The dashed line marks the He I-7065 Å rest frame position, while the dotted lines indicate the expansion velocity of  $\pm 1200$  km s $^{-1}$ .

days (see Table A4 and Figure 18), it becomes narrower with a terminal velocity of about  $1200$  km s $^{-1}$  (see Figure 9).

The flux evolution of the He I 6678 Å and 7065 Å lines reported in Figure 18 shows that the evolution of the line fluxes is consistent with that of the  $^{56}\text{Co}$  decay in the time interval  $+100 \div +300$  days, while at earlier and later phases some extra energy from the interaction between the ejecta and CSM is required.

Despite the CSM/ejecta interaction is likely the primary source for the SN luminosity, the mechanism responsible for the evolution of the He I emission is far from being clear. On day +449, the He I 7065 Å luminosity is  $\sim 4 \times 10^{38}$  erg s $^{-1}$ . The He I 5876 Å and He I 10830 Å lines are typically stronger than the He I 7065 Å line by 1.2 and 4–5 times, respectively (Almog & Netzer 1989). The total He I luminosity around day +450 is estimated to be  $\sim 2.8 \times 10^{39}$  erg s $^{-1}$ , which is larger than the total H $\alpha$  luminosity of  $2 \times 10^{39}$  erg s $^{-1}$  and significantly larger than the luminosity of the H $\alpha$  Core component. This fact and the low velocity of He-emitting gas suggest, again, that the helium emission originates from the He-rich central zone of the SN ejecta.

Interestingly, the H $\alpha$  line does not show a significant luminosity enhancement during  $+300 \div +450$  days (see Figure 10), when the He I 7065 Å flux increases by a factor of 4. This may be understood if the hydrogen ionisation fraction

**Table 4.** Main parameter values for SN 1996al progenitor systems

Name	Spectral type	$\log L_{H\alpha}$	Reference
SN 2009ip	SN-impostor/LBV	38.71 $^\dagger$	1
SN 2000ch	SN-impostor/LBV	38.48 $^{\dagger\dagger}$	2
UGC2773-2009OT	SN-impostor/LBV	38.38*	3
$\eta$ Car	LVB/O5.5III-O7I	37.55**	4
AG Car	LBV/B2/3Ib-WN11	37.54 $^\ddagger$	5
S Dor	LBV/A5Iaeq C	37.04 $^{\ddagger\ddagger}$	4
HR Car	LBV/B7Ve C	36.41*	4
$\zeta^1$ Sco	LBV/B1Ia-Oek C	35.32**	4
SN 1996al prog	—	37.28	This paper

$^\dagger$  Average values of three epochs (2010/10/06; 2011/09/02; 2011/09/24); assumed  $\mu = 31.55$  mag and  $E(B - V) = 0.019$  mag from Smith et al. (2010).

$^{\dagger\dagger}$  Average of two epochs (2000/05/06; 2009/05/19); assumed  $\mu = 30.17$  mag and  $E(B - V) = 0.013$  mag from Pastorello et al. (2010)

\* Average of three epochs (2012/07/20; 2009/09/05; 2010/01/26); assumed  $\mu = 28.95$  mag and  $E(B - V) = 0.5$  mag (only Galactic) from NED (<http://nedwww.ipac.caltech.edu>)

\*\* Measurements from the 2009/04/16 epoch; assumed distance of 2.3 kpc from Walborn (2012) and  $E(B - V) = 0.55$  mag from Humphreys & Martin (2012); spectral type from SIMBAD (<http://simbad.u-strasbg.fr/simbad/>)

$^\ddagger$  Average over eight years of measurements; assumed distance of 6 kpc from Humphreys et al. (1989); Hoekzema, Lamers, & van Genderen (1992) and  $E(B - V) = 0.65$  mag from Shore, Altner, & Waxin (1996); spectral type from SIMBAD

$^{\ddagger\ddagger}$  Average of four epochs (2008/02/04; 2009/02/08; 2009/09/15; 2010/08/03); assumed distance 49.97 kpc from Pietrzyński et al. (2013) for LMC and  $E(B - V) = 0.12$  mag from Massey (2000); spectral type from SIMBAD

\* Average of two epochs (2008/12/13 and 2010/04/01); assumed distance of 5 kpc and  $E(B - V) = 0.9$  mag from van Genderen et al. (1991); spectral type from SIMBAD

\*\* Average of two epochs (2009/10/19; 2010/07/04); assumed distance of 2 kpc and  $E(B - V) = 0.66$  mag from Crowther, Lennon, & Walborn (2006); spectral type from SIMBAD

1= Pastorello et al. (2013)

2= Pastorello et al. (2010)

3= Pastorello et al., in preparation

4= Richardson et al. (2012); Richardson, private communication

5= Stahl et al. (2001)

6= Herrmann et al. (2008)

is close to unity, so that the hydrogen emission does not react to the enhanced ionisation that leads to the emergence of strong helium lines. If this is the case, then the total mass of hydrogen in the SN ejecta should be close to the mass of the ionized hydrogen, i.e., of the order of  $0.1 - 0.3 M_\odot$  (see Sect. 3.5.1). Alternatively, if the helium is ionised by the central source, the X-UV radiation could be strongly attenuated already in the He layer, so that the external hydrogen layer would be only marginally affected.

Two possible sources for powering the transient He I emission are conceivable: X-ray emission from the enhanced CSM interaction or energy release due to accretion into the black hole. The latter requires the accretion of  $\sim 10^{-7} M_\odot$  during about +200 days and a super-Eddington X-UV luminosity. This could originate in the thermalisation of the

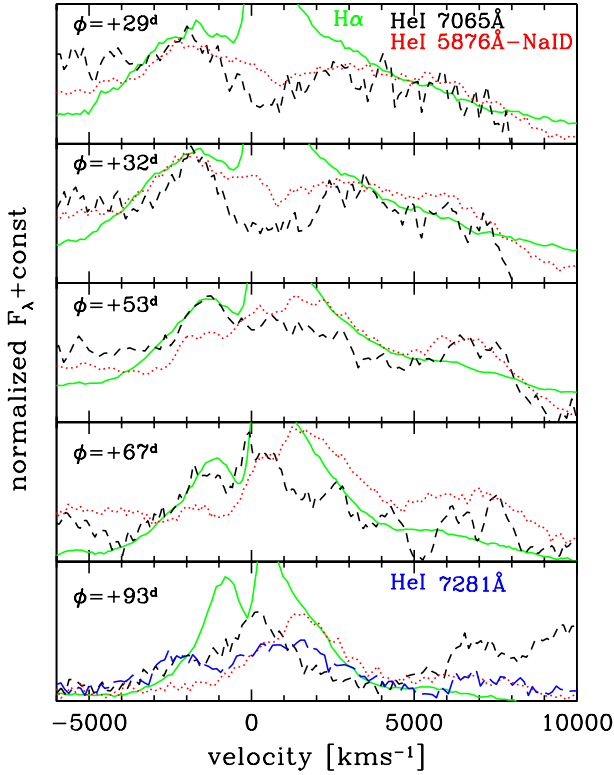


**Figure 16.** Comparison in the velocity space of the profile evolution of the He I 5876 Å - NaID feature (reference wavelength is 5876 Å, dotted, red lines) with those of the He I 7065 Å feature (short-dashed, black lines) and H $\alpha$  solid, green lines. In the last phase (+93 days), we also show the profile of He I 7281 Å feature (long-dashed, blue line).

accretion disk wind in a scenario of disk outflow interacting with the SN ejecta (Dexter & Kasen 2013).

### 3.4 Photospheric radius

In order to derive the evolution of the photospheric radius and temperature, we perform a blackbody fit to our early time spectra, after correcting for reddening and redshift values reported in Table 3. The fits were done selecting the portions of the spectra free of evident lines (examples of the fits are reported in Figure 6). The fit errors, which depend on a number of parameters, mainly the wavelength extension of the spectra, lines contamination, the uncertainty of the flux calibration and the assumed extinction, have been estimated to be of the order of 250 °K. Adopting the bolometric curve of Figure 4, spherical symmetry and a filling factor of 1, we estimate the evolution of the blackbody radius and the temperature (Figure 19). The computation is extended up to 100 days post explosion. This does not imply that the SN has a clear spheric symmetric photosphere up to that epoch (cfr. next Section).

The photosphere several days after the explosion is relatively hot, with a  $T_{BB} \sim 10000$  °K and a radius close

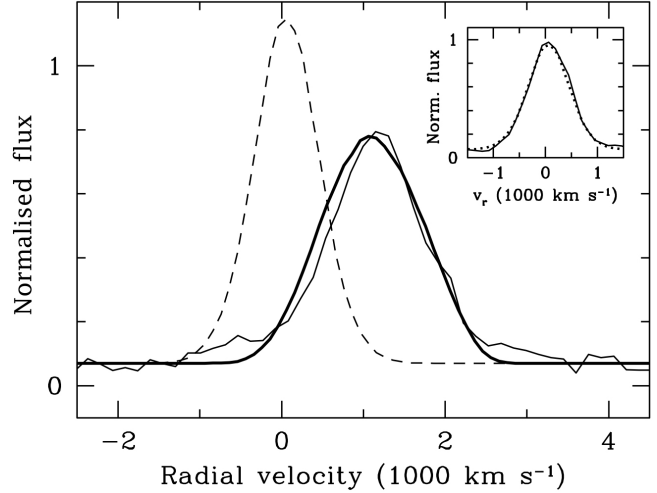


**Figure 17.** Effect of the non-local scattering of the He I 5876 Å emission by the NaID in SN 1996al. The observed spectrum on day +406 (*thin solid line*) is compared with the model spectrum (*thick solid line*). The latter is the result of the scattering of the mock-up He I 5876 Å emission (*dashed line*) in the optically thick NaID lines. The scaled mock-up He I 5876 Å profile (*dotted line*) is compared with the observed He I 7065 Å line in the *inset*. The radial velocity scale refers to the He I 5876 Å line.

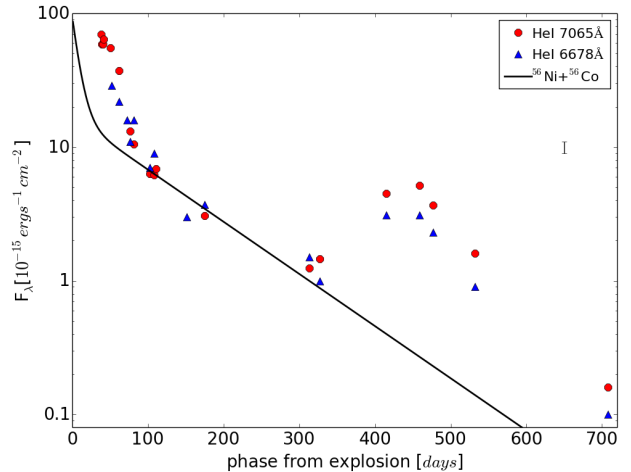


**Figure 18.** Flux evolution of the He I 6678 Å and 7065 Å lines. The fluxes have been reddening corrected. The  $^{56}\text{Ni}+^{56}\text{Co}$  fitting law is similar to that used for fitting the bolometric light curve of Figure 4 and has been tuned to fit the +100 ÷ +300 days flux points. As in Figure 4, a rise time to maximum of 10 days has been assumed. A mean error-bar for the line fluxes is reported.

to  $7.4 \times 10^{14}$  cm. While the temperature shows a smooth decrease to about 6500 °K at a phase of +100 days after explosion, the photospheric radius remains almost at a constant value of about  $6.9 \times 10^{14}$  cm up to 80 days after explosion, with a sudden decline to  $3.0 \times 10^{14}$  cm at phase about +100 ÷ +110 days (see Figure 19).

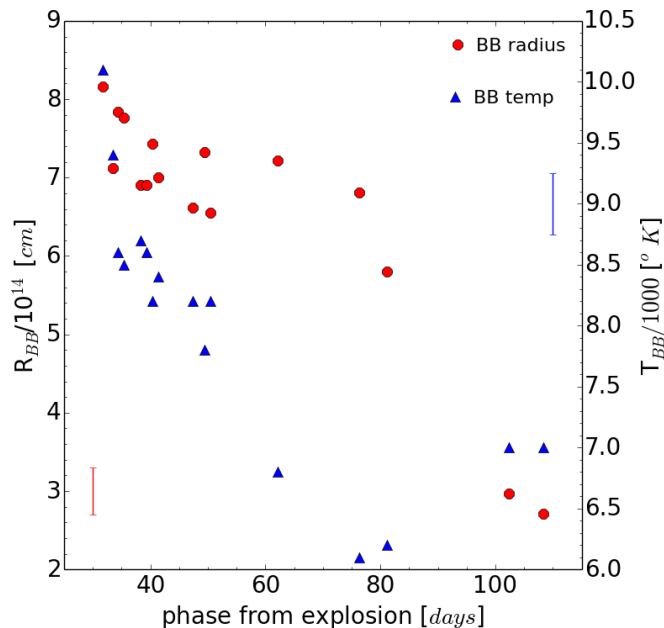


**Figure 19.** Evolution of the blackbody radius and the temperature in days from the explosion, assumed to occur 10 days before the maximum light. The average temperature error bar of  $\pm 250^\circ\text{K}$  is shown in the upper-right corner, while the mean error bar for radius ( $\pm 0.3 \times 10^{14}$  cm) is shown in the lower-left corner.

### 3.5 Parameters of the progenitor star and environment geometry

In the following, we will sketch a scenario for the SN explosion and its environment that will attempt to account for all available observations.

Despite a high expansion velocity of the ejecta ( $\sim 10^4$  km s $^{-1}$ , see Table A3) as indicated by the broad wing of H $\alpha$  and the boxy He I 5876 Å emission, the spectra have never shown pronounced broad absorption lines of either hydrogen or other species. This implies that the photosphere is located in the external layer of the SN ejecta. The absence of pronounced broad absorptions is typical of SNe II $_n$ , in which the SN ejecta interact with a dense circumstellar matter (CSM), and is attributed to the high optical depth in the cool dense shell (CDS), that is located at the ejecta/CSM interface (Chugai 2001). It should be emphasised that - in the case of SN 1996al - the CDS is probably patchy because we can detect the broad H $\alpha$  emission arising in the inner SN ejecta.

The higher resolution spectrum on day +43 (see Figure 7) showing the pronounced broad and narrow H $\alpha$  components can be used to probe both the SN ejecta and the CSM. The broad component is emitted by the freely expanding ejecta with maximum velocity of  $\lesssim 10000$  km s $^{-1}$ , while the narrow line with P-Cygni profile presumably forms in the CSM, which expands with  $v < 2000$  km s $^{-1}$ .

With these numbers, it is easy to calculate the radius of the CDS during the first 1-2 months after the explosion (assuming it occurred 10 days before the maximum light), which spans between  $3 - 4 \times 10^{15}$  cm. Given the radii calculated in the previous section, and supposing that the photosphere

is placed close to the CDS, an upper limit of  $\sim 10\%$  for the filling factor of the patchy CDS is derived.

#### 3.5.1 Modelling the early H $\alpha$ profile

The broad H $\alpha$  line is modelled with the Monte Carlo technique adopting the recombination emission in the ionised ejecta, with the H $^+$  and  $n_e$  distributions described by a broken power law ( $n_e \propto v^k$ ) with power index  $k = k_1$  in the inner zone ( $v < v_0$ ) and  $k = k_2$  in the outer zone. The Thomson scattering with thermal broadening in the ejecta is taken into account, assuming a kinetic temperature of  $10^4$  °K. Note that Thomson scattering turns out to be a crucial diagnostic probe for estimating the total amount of ionised hydrogen. Since our model does not compute the hydrogen level population, we consider two extreme cases for the H $\alpha$  optical depth: optically thin H $\alpha$  line ( $\tau_{23} \ll 1$ ) and optically thick one ( $\tau_{23} \gg 1$ ). The optically thin case is plausible, because the flux in the Balmer continuum seems to be large enough to strongly depopulate the second level. Two sources of continuum are included: the SN ejecta with the emissivity  $\epsilon \propto n_e^2$ , and the CDS at  $v = 10000$  km s $^{-1}$ . We do not compute the absolute flux neither in the line nor in the continuum. We neglect the contribution of the line emission from the CDS compared to the continuum radiation bearing in mind that, in the case of the opaque CDS, the contrast of the CDS line emission with respect to the CDS continuum is small. This is indicated by observations of interacting supernovae (e.g. SN 1998S at the age of 10-40 days, cf. Fassia et al. 2001) and supported by arguments based on the model of a thin opaque shell with the estimated line-to-continuum contrast of the order of the thermal-to-expansion velocity ratio (Chugai 2001). Instead, we let line and continuum emissivities of SN ejecta to fit the observations. The contribution of the CDS in the line emission is then neglected whereas the continuum radiation of the CDS is taken into account. The angular dependence of the CDS continuum brightness ( $I_c$ ) affects the strength of the H $\alpha$  broad absorption. We assume  $I_c \propto 1/\cos\theta$ , where  $\theta$  is the angle with the normal to the CDS surface. This approximation holds when the CDS is either optically thin or fragmented in such a way that the average number of clouds on the line of sight is less than unity. Strong fragmentation is expected given the fact that CDS is Rayleigh-Taylor unstable (Chevalier 1982). The contribution of the CDS continuum is a free parameter derived from the best fit of the H $\alpha$  profile. The latter, is determined by the normalised distribution of ionised hydrogen along the radius and by the Thomson optical depth.

We show two cases for the broad component:  $\tau_{23} \ll 1$  (no H $\alpha$  resonance scattering) and  $\tau_{23} \gg 1$  (Figure 20). A reasonable fit of the broad component to the observed H $\alpha$  profile on day +43 is found for the parameters:  $k_1 = 1$ ,  $k_2 = -1.7$ ,  $v_0 = 1800$  km s $^{-1}$ , and Thomson optical depth  $\tau_T = 2.1$ . The case without Thomson scattering (dotted line in Figure 20a) demonstrates the crucial role of electron scattering for the formation of the line profile. In the case of the optically thick H $\alpha$  line, we find that the relative contribution of the ejecta continuum is  $\leq 10\%$ ; for a larger contribution of the ejecta continuum, the broad H $\alpha$  absorption component becomes prominent. For the optically thin H $\alpha$ , the calculated recombination continuum in the Case B, can contribute only to 3.3% of the observed continuum. The

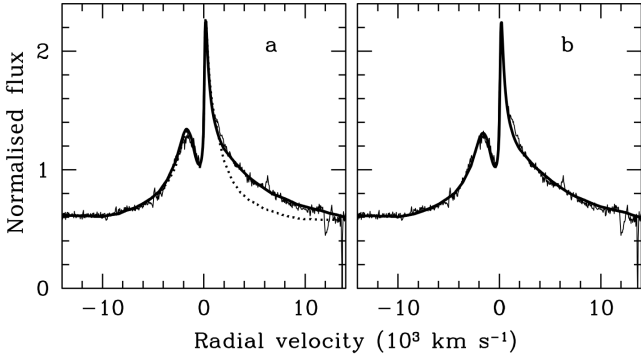


**Figure 20.** Comparison of the  $H\alpha$  line model with the observed spectrum on day +43 (*thin solid line*). *Panel a:* the SN ejecta with optically thin  $H\alpha$  line (*thick solid line*) and the same model without Thomson scattering (*dotted line*). *Panel b:* model with optically thick  $H\alpha$  line. In both cases the narrow component forms in the CSM and is primarily due to resonance scattering.

recovered Thomson optical depth, together with the estimated CDS radius on day +43 and the normalised electron distribution recovered from the  $H\alpha$  profile, suggest a mass of ionised hydrogen of  $0.07 M_{\odot}$  in the ejecta and a  $H\alpha$  luminosity of  $2 \times 10^{40} \text{ erg s}^{-1}$  on day +43. The latter is in excellent agreement with the observational estimate.

We now turn to the narrow line. The peak of the narrow emission on days +23 and +43 suggests the presence of the  $H\alpha$ -emitting circumstellar gas with velocities of  $\sim 300 \text{ km s}^{-1}$ . On the other hand, the wings of the narrow emission profile and the blue edge of the narrow absorption indicate CSM velocities as high as  $\sim 2000 \text{ km s}^{-1}$ . This is consistent with the expansion law  $v \propto r$  for the CSM with a maximum velocity of  $\sim 2000 \text{ km s}^{-1}$  which is used for the  $H\alpha$  modeling. We adopt the external radius for the fast CSM outflow of  $5 \times 10^{15} \text{ cm}$  on day +43, keeping in mind that the spectra suggest that this kinematics is maintained at least until day +63. We find that the resonance scattering is a good approximation for the narrow P-Cygni line, although we need to add a net emission which amounts to 8% of the resonant scattering component. We checked also a model where the CSM outflow has a constant velocity. However, such a model reproduced neither the absorption nor the emission components of the narrow line. In the best-fit case shown in Figure 20, the  $H\alpha$  optical depth in the CSM decreases outward from 0.9 at the CDS radius ( $R_s$ ) down to zero at the boundary radius  $R_b$  according to  $\tau = 0.9[(r - R_s)/(R_b - R_s)]^{1.6}$ .

The kinematics  $v \propto r$  followed by the observed narrow  $H\alpha$  poses a question about its origin. Generally, this sort of the kinematics combined with large value of the terminal velocity ( $\sim 2000 \text{ km s}^{-1}$ ) suggests a mass ejection via shock wave. At present, we are not able to propose a reliable mechanism for this vigorous mass loss. Beside the stellar shock, the common envelope phase in a binary system could also play a role.

### 3.5.2 Modelling the light curve

The fast initial ( $t < +100$  days) drop of the bolometric light curve (see Figure 4) strongly indicates that the diffusion time in the SN envelope is small, which implies low-mass ( $\sim 1 M_{\odot}$ ) ejecta. At first glance, this is at odds with the high

mass of the SN progenitor suggested by the pre-explosion  $H\alpha$  luminosity ( $\sim 10^{37} \text{ erg s}^{-1}$ , see Table 4). In fact, in the case B recombination, the pre-explosion  $H\alpha$  requires a rate of ionising radiation of  $\sim 10^{49} \text{ photons s}^{-1}$ . To sustain this ionisation rate, we need a hot progenitor star with bolometric luminosity  $\log L/L_{\odot} \gtrsim 5.4$  and radius  $R \sim 10 R_{\odot}$  (see discussion in Sect. 3.1). According to atmosphere models (Simón-Díaz & Stasińska 2008), the above precursor may have been a  $25 M_{\odot}$  ZAMS star at the final evolutionary stage (Woosley, Heger, & Weaver 2002). The apparent controversy between the SN light curve and pre-SN  $H\alpha$  constraints can be solved if one assumes that the  $25 M_{\odot}$  ZAMS progenitor had lost almost the whole hydrogen envelope, with most of the helium core falling back onto the collapsing core making a black hole (see models in the  $25 - 30 M_{\odot}$  mass range of Heger et al. 2003).

For our fiducial model we assume that the  $25 M_{\odot}$  progenitor (Woosley, Heger, & Weaver 2002) ends up as a stripped pre-SN star with a  $8.3 M_{\odot}$  helium core, and a  $0.3 M_{\odot}$  envelope, with a hydrogen mass fraction of 0.5. The adopted pre-SN radius is  $R = 10 R_{\odot}$  constrained by the pre-explosion  $H\alpha$  luminosity. To construct the stripped pre-SN configuration, we scaled the mass and the radius of the hydrogen envelope of the  $25 M_{\odot}$  progenitor to the required values. Using a radiation hydrodynamics code (Utrobin 2007; Utrobin et al. 2015), we analysed the outcome of the explosion which is initiated by a supersonic piston applied to the bottom of the stellar envelope at the boundary of the  $2.1 M_{\odot}$  central core, which is then removed from the computational mass domain and assumed to collapse into a neutron star. We computed a set of SN models with explosion energies of  $(0.1 - 1.0) \times 10^{51} \text{ erg}$ , ejecta masses of  $0.45 - 2.1 M_{\odot}$ , and kinetic energies of  $(0.2 - 4.5) \times 10^{50} \text{ erg}$ . Note that the explosion energies released at the boundary of the collapsing core are in the plausible range for the neutrino-driven explosion mechanism (Janka 2012). The light curves of these models have a very narrow shock breakout peak ( $\sim 10^{-4}$  days), a short overall duration ( $\sim 10$  days), and a luminosity of  $< 10^{42} \text{ erg s}^{-1}$  (after the shock breakout peak), while the expansion velocity at the boundary is large ( $> 10^4 \text{ km s}^{-1}$ ). These properties are in agreement with the absence of broad absorption lines in the spectra which, in turn, suggest a small energy contribution of the intrinsic SN luminosity to the bolometric light curve, and instead support the circumstellar interaction as the dominant source powering the SN luminosity.

The bolometric luminosity powered by the CS interaction is calculated in a thin shell approximation (Chevalier 1982; Chugai 2001). The model suggests that freely expanding SN ejecta collide with dense CSM. The interaction proceeds via forward and reverse shocks with the CDS at the contact boundary between SN and CSM. The CDS radius  $R_s$  and velocity  $v_s$  are recovered from the numerical solution of the equations of motion and mass conservation. The forward shock velocity is  $v_s - v_w$  ( $v_w$  is the wind velocity) and the reverse shock velocity is  $R/t - v_s$ . The post-shock temperature is set by the shock velocity assuming an isothermal ( $T_e = T_i$ ) strong shock, while the post-shock density is set to be four times the pre-shock density. The X-ray luminosity of the  $j$ -th shock ( $j = 1$  for the forward shock and  $j = 2$  for the reverse shock) is  $L_j = 2\pi R_s^2 v_j^3 \eta_j$ , where  $v_j$  is the shock velocity,  $\eta_j = t/(t + t_{c,j})$  is the cooling efficiency and  $t_{c,j}$



is the post-shock cooling time. The optical bolometric luminosity is calculated assuming that the full X-ray luminosity of both shocks is absorbed by the cool material of the CDS, the un-shocked SN ejecta and the CSM.

We consider two cases: (i) spherically symmetric CSM with velocities  $v = v_0(r/r_0)$  for  $r < r_0$  and  $v = v_0 = 2000 \text{ km s}^{-1}$  for  $r > r_0 \approx 5 \times 10^{15} \text{ cm}$  and (ii) anisotropic CSM with a dense equatorial disk and a rarefied, more symmetric flow. This latter outflow presumably does not contribute significantly to the interaction luminosity, although it is responsible for the narrow H $\alpha$  absorption. The equatorial CSM is assumed to have a low expansion velocity: we set it to be  $100 \text{ km s}^{-1}$  (the result does not depend on the exact value of  $v_w$ ). The CSM anisotropy is set as the fraction of a sphere occupied by the equatorial CSM,  $G = \Omega(r)/4\pi$ . This factor multiplied by the luminosity computed for the spherical CSM gives the luminosity in the anisotropic case. Indeed, the luminosity and its temporal evolution constrain the CS density and its radial distribution. We find that the requirement of a rapid deceleration suggests a low mass and low energy supernova ejecta in order to minimise the ejecta momentum. A search for the best fit model in an extended parameter space leads us to conclude that one cannot describe simultaneously the light curve and the low expansion velocity in the framework of a spherically symmetric model. This is the primary reason to invoke an asymmetric CSM. We do not pursue the goal to find the best fit model for the CSM using a minimisation procedure. Our best-fit model should be considered rather as a reasonable possibility.

The model light curves and the expansion velocity of the CDS for the isotropic and anisotropic CSM cases are shown in Figure 21. As parameters for the hydrodynamical model we adopt an ejecta mass  $M = 1.15 M_\odot$  and a kinetic energy  $E = 1.6 \times 10^{50} \text{ erg}$ . The ejecta consist of  $0.15 M_\odot$  of hydrogen and nearly  $1.0 M_\odot$  of helium. The rest of the He core is assumed to fall back, thus possibly making a black hole with a mass of  $7-8 M_\odot$ . The SN explosion produces the brief shock breakout peak followed by a short quasi-plateau ( $\sim 12$  days) with a luminosity of  $\sim 10^{41} \text{ erg s}^{-1}$ . This contributes negligibly to the SN luminosity, which is instead dominated by CS interaction (Figures 21, panels a and c). The modelled interaction luminosity for both the spherical and the anisotropic CSM well fits the observed light curve (Figures 21, panels a and c), whereas the expansion velocities of the CDS at late times are quite different: the spherical model predicts deceleration down to  $3000 \text{ km s}^{-1}$ , while the CDS for the equatorial CSM is decelerated down to  $1300 \text{ km s}^{-1}$  (Figures 21, panels b and d). In that respect, the non-spherical model is preferred, given the similarities of the model with the velocity evolution of H $\alpha$  and the He I lines shown in Figure 9. The total mass of the non-spherical CSM in the range of  $r < 3 \times 10^{16} \text{ cm}$  is  $0.13 M_\odot$ . The geometric factor is  $G = 0.02$  at the large radii (Figure 21d, inset) which corresponds to a polar angle width of the equatorial disk of  $23^\circ$ .

The scenario with an equatorial CSM predicts a double-horn line emitted in the interaction zone. Indeed, at  $t > +142$  days the H $\alpha$  shows Blue and Red bumps with radial velocities of about  $-1100 \text{ km s}^{-1}$  and  $1550 \text{ km s}^{-1}$ , respectively (see Table A4). The velocity and intensity differences between those peaks indicate that the structure of the CSM deviates from axial symmetry.

### 3.5.3 Evidence from narrow absorption lines

The narrow absorptions of the H $\alpha$ , H $\beta$ , and Fe II (mult. 42) lines are shallow in the higher resolution spectra of days +23 to +26 (see Sect. 2.4). Moreover, H $\alpha$  and H $\beta$  have similar relative depths,  $A \approx 0.1$ . Given a theoretical ratio of optical depths H $\beta$ /H $\alpha = 1/7$ , the facts that the H $\beta$  and H $\alpha$  absorptions have similar depths and are both shallow imply that these lines are saturated, but only about 10% of the continuum source is covered by line absorbers. The spherical component of the CSM responsible for the narrow absorptions is therefore clumpy and consists of clouds optically thick in the H $\alpha$  and H $\beta$  lines embedded in the optically thin inter-cloud gas. The interaction with the clumpy spherical CSM might contribute to the central (Core) H $\alpha$  emission component ( $t > 142 \text{ d}$ ). The fact that this emission component is redshifted by  $300-400 \text{ km s}^{-1}$  could be attributed to the asymmetry of the CSM in a sense that the far side of the quasi-spherical CSM is more dense and mostly contributes to the Core H $\alpha$  emission.

### 3.5.4 The progenitor scenario

The dominant role of the continuum originated by the CSM-ejecta interaction and the significant deceleration of the SN ejecta indicate lower ejecta mass and explosion energy than in normal core-collapse SNe. We have shown in the previous Sect. that ejecta with  $M_{ej} \approx 1.15 M_\odot$  and  $E \approx 1.6 \times 10^{50} \text{ erg}$  are consistent with the observations. The low hydrogen mass ( $\sim 0.15 M_\odot$ ) and the high He I luminosity around day +450 imply that the ejecta are made up primarily of helium ( $\sim 0.8 M_\odot$ ).

The CSM close to the exploding star has an overall spherical distribution (see Figure 22), but with some density enhancement in an oblate structure to explain the asymmetric, early He I line profiles. The inner radius of the equatorial disk is  $r \approx 3 \times 10^{15} \text{ cm}$ , while its external limit is  $> 5 \times 10^{17} \text{ cm}$  ( $> 0.15 \text{ pc}$ ), since the ejecta are still interacting with the disk at the time of our last observation (+5542 day). The disk is embedded in a more spherically symmetric, clumpy CSM. The mass of the CSM in the anisotropic model, including the inner mostly spherical zone is  $0.13 M_\odot$ , within a distance  $r < 3 \times 10^{16} \text{ cm}$ . This value is very similar to the amount of CS mass found in the twin SN 1994aj (Paper I) and about ten times more than in SN 1996L (Paper II). According to this scenario, and given the progressive quenching of the H $\alpha$  Core and Red components, we may suppose that both the receding part of the disk and the quasi-symmetric, clumpy CSM get shallower and shallower in density with time, or that some obscuring dust is forming mostly inside the shocked ejecta (or a combination of the two).

The presence of dense CSM around the progenitor star of SN 1996al is also supported by the recovery of the progenitor in an archive H $\alpha$  image, from which a H $\alpha$  luminosity of  $\log L_{H\alpha} \sim 37.28$  is derived. This H $\alpha$  luminosity implies a massive  $\sim 25 M_\odot$  ZAMS progenitor star (see Sect. 3.1), which has lost almost the entire hydrogen envelope during its evolution.

It is interesting to note that such a highly asymmetric geometric configuration derived for the SN 1996al CSM has been observed around very massive evolved stars such as MN18 of Large Magellanic Cloud (LMC), and in other blue

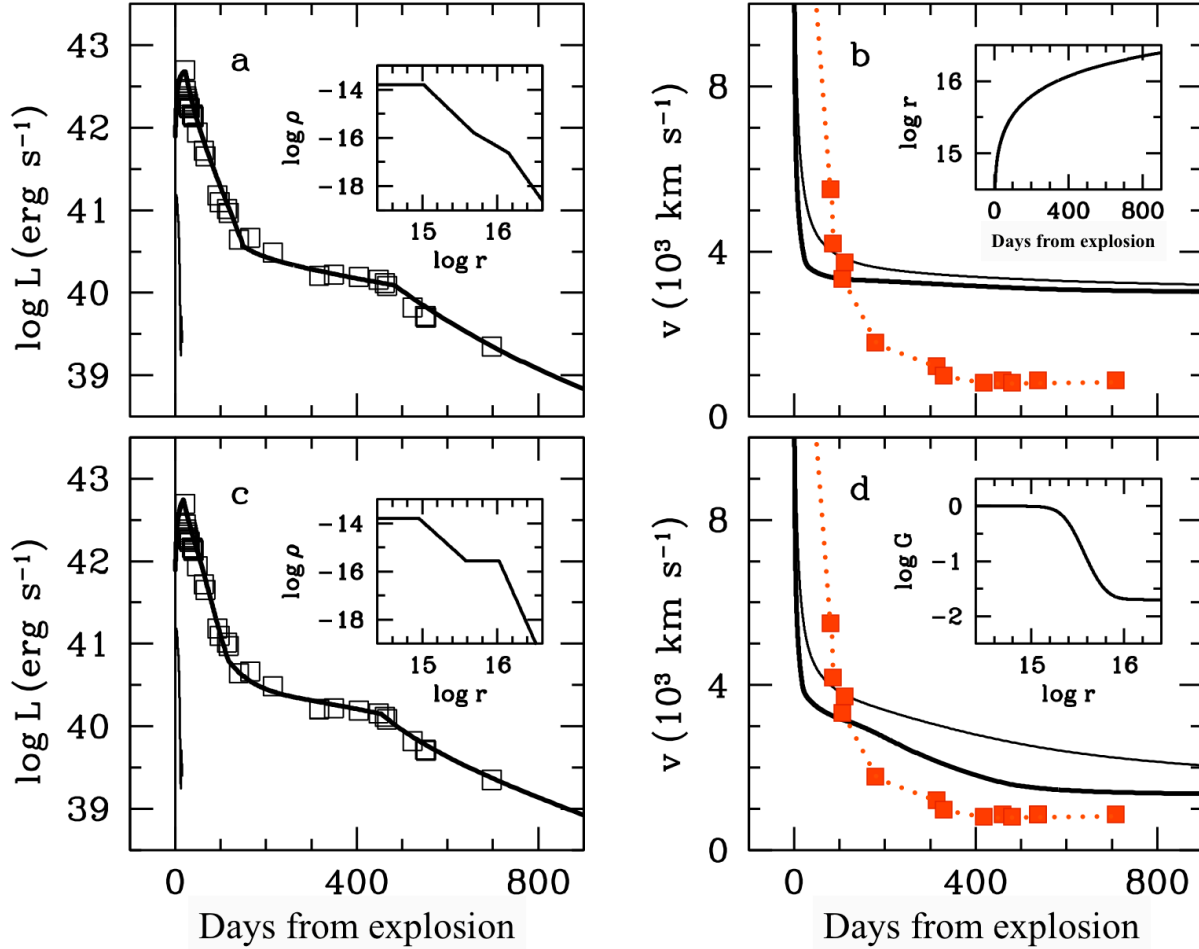


**Figure 21.** Bolometric light curve and expansion velocity in the CS interaction model. *Panel a:* light curves of the fast evolving, dim hydrodynamic model (*thin line*) and the interaction model (*thick line*) in the spherical case compared to the observations (*open squares*). The inset shows the CS density distribution, where  $\rho$  and  $r$  units are  $\text{g cm}^{-3}$  and cm, respectively. *Panel b:* the CDS velocity (*thick line*) and the boundary velocity of the un-shocked SN ejecta (*thin line*). For comparison, the observed velocities of the He I 7065 Å are also plotted (*solid, red squares* connected with a *dotted, red line*). The inset shows the CDS radius. *Panel c:* the same as in panel *a* but for the non-spherical case. *Panel d:* the CDS velocity (*thick line*) and the boundary velocity of the un-shocked SN ejecta in the equatorial plane (*thin line*). For comparison, the observed velocities of the He I 7065 Å are also plotted (*solid, red squares* connected with a *dotted, red line*). The inset shows the geometric factor describing the angular width of the equatorial disk (see text).

supergiants (including LBV candidates) of LMC and Milky Way, including the SN 1987A’s progenitor (Gvaramadze et al. 2015).

In this scenario, the absence of [O I] 6300-6364 Å emission lines at any phase (see Figure 23) is naturally explained since most of the oxygen layer has fallen onto the black hole<sup>5</sup>.

<sup>5</sup> It is interesting to note that a similar scenario (low energy,  $4 \times 10^{50}$  erg; massive,  $26 M_{\odot}$ , progenitor; substantial fallback of material on to the collapsed core) has been proposed to explain the physical characteristics of SN 1997D (Turatto et al. 1998; Benetti et al. 2001). However, this high mass scenario has been questioned by Chugai & Utrobin (2000) who, instead, proposed a low mass progenitor for SN 1997D. In the case of SN 1996al the key parameter that point towards a high mass progenitor scenario is the pre-explosion H $\alpha$  luminosity.

## 4 CONCLUSIONS

Extensive photometric and spectroscopic observations of SN 1996al along 15 years of its evolution are presented. The light curve indicates that the SN is of Type III, reaching peak absolute magnitudes of  $M_B \sim -18.6$  and  $M_V \sim -18.2$ . However, a closer inspection shows that the decline rate changes with time, and this is correlated with significant changes in the spectral appearance. The complex SN evolution is very likely a consequence of the primary role played by the ejecta-CSM interaction during all phases of the SN life.

The spectra obtained soon after the maximum light show narrow P-Cygni Balmer lines superimposed on broader components with asymmetric profiles. In addition, broad and asymmetric He I lines in emission are detected. At these early phases, the broad H component and the He lines form in the same outer region of the ejecta. By day +142, the H $\alpha$  profile dramatically changes: the narrow emission component disappears, and H $\alpha$  splits in three components of

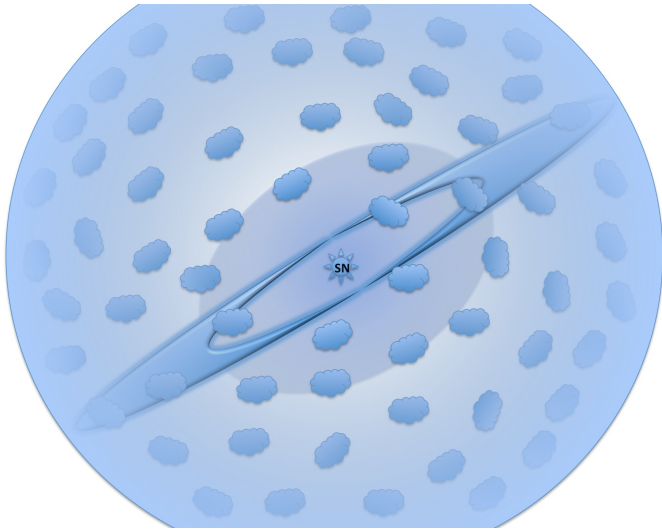


**Figure 22.** Schematic cartoon of the CSM shape surrounding SN 1996al (not to scale). Line of sight is perpendicular to the figure plane. See text for a description.

comparable widths, that remain at constant wavelengths afterward. This composite profile remains visible over 15 years, although the relative strengths of the three components change with time.

The He lines behave differently. After day +100, they become significantly narrower ( $\leq 1000 \text{ km s}^{-1}$ ) and symmetric, a clear indication that they form in a different region of the ejecta. Later on, between day +300 and +600, they experience a sudden increase in flux. Then, the flux of the He I line decreases again, and by day +700, these lines fade below the detection threshold.

We have also recovered information on the progenitor star by inspecting a pre-explosion archive image in the  $\text{H}\alpha$  narrow band. A luminous source is detected at the location of SN 1996al, showing a total  $\text{H}\alpha$  luminosity of  $1.9 \times 10^{37} \text{ erg s}^{-1}$ , which favours a massive ( $25 M_{\odot}$  ZAMS) progenitor star for SN 1996al. This, along with the SN parameters derived by the modelling, suggests that the progenitor was stripped of a large fraction of the hydrogen envelope in the latest stages of its life which ended with the collapse of a  $7 - 8 M_{\odot}$  helium core.

The peculiar evolution of the H and He I lines is likely a consequence of the geometry, the non-uniform density profile of the CSM surrounding SN 1996al and the fallback onto the compact remnant. Observational evidences favour an highly structured CS scenario characterised by inner, high-density material with oblate structure plus an equatorial ring extended over  $0.15 \text{ pc}$ , both embedded in a more spherically symmetric, lower-density but clumpy CSM. The total mass of the CSM is modest, being  $\gtrsim 0.13 M_{\odot}$  within a distance  $\lesssim 3 \times 10^{16} \text{ cm}$ .

Models show that the luminosity of SN 1996al is best sustained by SN ejecta-CSM interaction. The inferred ejected mass is relatively small ( $\sim 1.15 M_{\odot}$ ,  $\sim 0.15 M_{\odot}$  of which is hydrogen, the residual fraction is helium) and is expelled in a low kinetic energy explosion ( $\sim 1.6 \times 10^{50} \text{ erg}$ ). The amount of ejected  $^{56}\text{Ni}$  (if any) expelled in the explosion is constrained to be  $\lesssim 0.018 M_{\odot}$ . The modest ejecta and

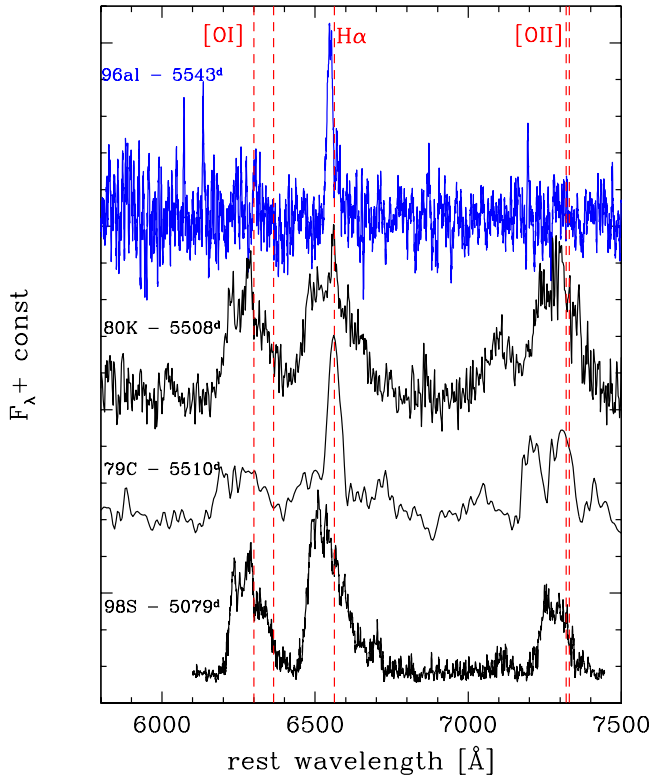


**Figure 23.** Comparison of spectra taken about 14 years after explosion of our SNe sample. The SNe 1979C and 1980K spectra are from Fesen et al. (1999), while that of SN 1998S is from Mauerhan & Smith (2012).

$^{56}\text{Ni}$  mass are explained with a massive fallback of material into the compact remnant, producing a  $7 - 8 M_{\odot}$  black hole.

## ACKNOWLEDGMENTS

We thank the anonymous referee for very useful comments and suggestions.

We thank T. Augusteijn, M. Birlan, J. F. Le Borgne, S. Covino, P. Rosati and G. C. Van de Steene for giving us part of their telescope time; P. Fouqué for supplying the DENIS photometry; and M. Riello for performing some of the observations.

We are in debt with N. Richardson for providing unpublished spectra of LBVs.

We thank R. McCray and J. Marcaide for helpful discussions and comments on the manuscript.

SB, MT, AP are partially supported by the PRIN-INAF 2014 project Transient Universe: unveiling new types of stellar explosions with PESSTO. VPU is supported by Russian Scientific Foundation grant 14-12-00203. NC thanks the Program of RAS "Explosions in Astrophysics" for financial support. G.P. acknowledge support provided by the Millennium Institute of Astrophysics (MAS) through grant IC120009 of the Programa Iniciativa Científica Milenio del Ministerio de Economía, Fomento y Turismo de Chile.

This work is based on observations collected at the ESO-La Silla (under programs ESO N° 151.D-0004, 56.D-0478, 57.D-0534, 58.D-0307, 59.D-0332, 60.D-0415, 61.D-0630, 57.E-0646); and ESO-Paranal (under programs ESO N° 67.D-0422, 073.D-0670, 080.D-0213, 084.D-0265, 087.D-0693) Observatories.

One spectrum has been collected at the Anglo Australian Observatory by R. Stathakis, B. Schmidt and S. Woodings and retrieved via AAT Archive ([http://apm5.ast.cam.ac.uk/arcbin/wdb/aat\\_database/observation\\_log/make](http://apm5.ast.cam.ac.uk/arcbin/wdb/aat_database/observation_log/make)).

This research has made use of the NASA/IPAC Extragalactic Database (NED) which is operated by the Jet Propulsion Laboratory, California Institute of Technology, under contract with the National Aeronautics and Space Administration. We have also made use of the Lyon-Meudon Extragalactic Database (LEDA), supplied by the LEDA team at the Centre de Recherche Astronomique de Lyon, Observatoire de Lyon.

## REFERENCES

- Almog, Y., & Netzer, H. 1989, MNRAS, 238, 57
- Aretxaga, I., Benetti, S., Terlevich, R. J., et al. 1999, MNRAS, 309, 343
- Barbon R., Ciatti F., Rosino L., 1982, A&A, 116, 35
- Benetti, S., & Neuhauser, R. 1996, IAUC, 6438, 1
- Benetti, S., Cappellaro, E., Danziger, I. J., et al. 1998, MNRAS, 294, 448 (Paper I)
- Benetti S., Turatto M., Cappellaro E., Danziger I. J., Mazzali P. A., 1999, MNRAS, 305, 811 (Paper II)
- Benetti, S., Turatto, M., Balberg, S., et al. 2001, MNRAS, 322, 361
- Branch D., Falk S. W., Uomoto A. K., Wills B. J., McCall M. L., Rybski P., 1981, ApJ, 244, 780
- Buonanno, R., Buscema, G., Corsi, C. E., Ferraro, I., Iannicola, G., 1983, A&A, 126, 278
- Buta R. J., 1982, PASP, 94, 578
- Caldwell N., Kennicutt R., Phillips A. C., Schommer R. A., 1991, ApJ, 370, 526
- Cappellaro E., Danziger I. J., della Valle M., Gouiffes C., Turatto M., 1995, A&A, 293, 723
- Cardelli J.A., Clayton G.C. Mathis J.S., 1989, ApJ, 345, 245
- Chandrasekhar, S. 1960, New York: Dover, 1960
- Chevalier, R. A. 1982, ApJ, 259, 302
- Chevalier, R. A., & Fransson, C. 1994, ApJ, 420, 268
- Chugai N.N. 1990, SvA, 16, L457
- Chugai, N. N., & Utrobin, V. P. 2000, A&A, 354, 557
- Chugai, N. N. 2001, MNRAS, 326, 1448
- Crowther P. A., Lennon D. J., Walborn N. R., 2006, A&A, 446, 279
- Danziger I. J., 1988, in Greco M., ed., Results and Perspectives in Particle Physics. Editions Frontieres, France, p. 3
- Dexter, J., & Kasen, D. 2013, ApJ, 772, 30
- Doggett, J.B., Branch, D., 1985, AJ 90, 2303
- Evans R., Benton R., Beaman S., Pogson J., Ryan S., 1996, IAUC, 6437, 1
- Faran, T., Poznanski, D., Filippenko, A. V., et al. 2014, MNRAS, 445, 554
- Fassia, A., Meikle, W. P. S., Vacca, W. D., et al. 2000, MNRAS, 318, 1093
- Fassia, A., Meikle, W. P. S., Chugai, N., et al. 2001, MNRAS, 325, 907
- Fesen, R.A., et al. 1999, AJ, 117, 725
- Freedman W. L., Madore B. F., Gibson B. K., et al., 2001, ApJ, 553, 47
- Gvaramadze, V. V., Kniazev, A. Y., Bestenlehner, J. M., et al. 2015, MNRAS in press, arXiv:1508.06288
- Heger, A., Fryer, C. L., Woosley, S. E., Langer, N., & Hartmann, D. H. 2003, ApJ, 591, 288
- Herrmann, K. A., Ciardullo, R., Feldmeier, J. J., & Vinciguerra, M. 2008, ApJ, 683, 630
- Hoekzema N. M., Lamers H. J. G. L. M., van Genderen A. M., 1992, A&A, 257, 118
- Humphreys R. M., Lamers H. J. G. L. M., Hoekzema N., Cassatella A., 1989, A&A, 218, L17
- Humphreys R. M., Martin J. C., 2012, ASSL, 384, 1
- Janka, H.-T. 2012, Annual Review of Nuclear and Particle Science, 62, 407
- Karachentsev I. D., Sharina M. E., Huchtmeier W. K., 2000, A&A, 362, 544
- Kennicutt R. C., Hodge P. W., 1980, ApJ, 241, 573
- Kraan-Korteweg R. C., 1986, A&AS, 66, 255
- Landolt A. U., 1992, AJ, 104, 340
- Liu, Q.-Z., Hu, J.-Y., Hang, H.-R., et al. 2000, A&AS, 144, 219
- Massey P., 2000, PASP, 112, 144
- Mauerhan, J., & Smith, N. 2012, MNRAS, 424, 2659
- Oke, J. B. 1990, AJ, 99, 1621
- Osterbrock, D. E. 1989, Research supported by the University of California, John Simon Guggenheim Memorial Foundation, University of Minnesota, et al. Mill Valley, CA, University Science Books, 1989, 422 p.
- Pastorello A., et al., 2013, ApJ, 767, 1
- Pastorello A., et al., 2010, MNRAS, 408, 181
- Patat, F., Barbon, R., Cappellaro, R., Turatto, M., 1994, A&A 282, 731
- Pietrzyński G., et al., 2013, Nature, 495, 76
- Richardson N. D., Gies D. R., Morrison N. D., Schaefer G., ten Brummelaar T., Monnier J. D., Parks J. R., 2012, ASPC, 465, 160
- Schlegel D. J., Finkbeiner D. P., Davis M., 1998, ApJ, 500, 525
- Shore S. N., Altner B., Waxin I., 1996, AJ, 112, 2744
- Simón-Díaz, S., & Stasińska, G. 2008, MNRAS, 389, 1009
- Smartt, S. J. 2009, ARA&A, 47, 63
- Smith N., et al., 2010, AJ, 139, 1451
- Stahl O., Jankovics I., Kovács J., Wolf B., Schmutz W., Kaufer A., Rivinius T., Szeifert T., 2001, A&A, 375, 54
- Stetson, P. B. 1992, in Astronomical Data Analysis Software and Systems I, D.M. Worall, C. Biemesderfer, and J. Barnes, San Francisco: Astronomical Society of the Pacific, 297
- Terlevich R. J., 1994, in Clegg R. E. S., Stevens I. R., Meikle W. P. S., eds, Circumstellar Media in the Late Stages of Stellar Evolution. Cambridge Univ. Press, Cambridge p. 153
- Tsvetkov D. Y., 1983, PZ, 22, 39
- Turatto, M., Cappellaro, E., Danziger, I. J., et al. 1993, MNRAS, 262, 128
- Turatto, M., Mazzali, P. A., Young, T. R., et al. 1998,

- ApJL, 498, L129
- Turatto M., Benetti S., Cappellaro E., 2003, in the proceedings to the ESO/MPA/MPE Workshop (an ESO Astrophysics Symposium) *From Twilight to Highlight: The Physics of Supernovae*, eds. B. Leibundgut and W. Hillebrandt (Springer-Verlag), p.200
- Uomoto A., Kirshner R. P., 1986, ApJ, 308, 685
- Utrobin, V. P. 2007, A&A, 461, 233
- Utrobin, V. P., Wongwathanarat, A., Janka, H.-T., Müller, E. 2015, A&A, 581, A40
- van Genderen A. M., Robijn F. H. A., van Esch B. P. M., Lamers H. J. G., 1991, A&A, 246, 407
- Vernet, J., Dekker, H., D'Odorico, S., et al. 2011, A&A, 536, A105
- Walborn N. R., 2012, ASSL, 384, 25
- Willick, J. A., Courteau, S., Faber, S. M., et al. 1997, ApJS, 109, 333
- Woosley S. E., Hartmann D., Pinto P. A., 1989, ApJ, 346, 395
- Woosley, S. E., Heger, A., & Weaver, T. A. 2002, Reviews of Modern Physics, 74, 1015

## APPENDIX A:

### A1 Light curves and spectroscopic log of SN 1996al

**Table A1.** Optical and NIR photometric measurements for SN 1996al.

date	MJD	ph days <sup>†</sup>	<i>U</i>	<i>B</i>	<i>V</i>	<i>R</i>	<i>I</i>	<i>J</i>	<i>H</i>	tel.	seeing arcsec
23/7/96	50287.29	22.8	14.27(08)	14.80(05)	14.61(04)	14.37(04)	14.25(04)			Dut	1.3
25/7/96	50289.32	24.8	14.54(07)	14.98(09)	14.77(03)	14.48(03)	14.36(03)			Dut	2.0
26/7/96	50290.34	25.8	14.68(05)	15.05(04)	14.81(03)	14.56(03)	14.42(03)			Dut	1.7
27/7/96	50291.35	26.9	14.76(05)	15.13(04)	14.90(03)	14.62(03)	14.49(03)			Dut	2.4
28/7/96	50292.32	27.8	14.88(05)	15.19(04)	14.96(03)	14.69(03)	14.56(02)			Dut	1.7
29/7/96	50293.33	28.8	14.96(04)	15.26(03)	15.01(04)	14.72(03)	14.60(04)			Dut	1.6
29/7/96	50293.40	28.9						14.27(05)		Den	—
30/7/96	50294.40	29.9	15.03(09)	15.34(05)	15.03(02)	14.75(04)	14.62(02)			Dut	1.4
1/8/96	50296.31	31.8	15.00(08)	15.36(05)	15.11(02)	14.81(03)	14.70(02)			Dut	2.2
6/8/96	50301.30	36.8	15.31(09)	15.55(04)	15.25(03)	14.95(03)	14.83(03)			Dut	1.5
7/8/96	50302.28	37.8	15.32(07)	15.57(04)	15.28(03)	14.94(03)	14.82(03)			Dut	2.3
7/8/96	50302.43	37.9			15.29(03)					EF1	1.5
8/8/96	50303.43	38.9			15.26(02)					EF1	2.4
9/8/96	50304.43	39.9			15.27(03)					EF1	1.9
10/8/96	50305.27	40.8			15.27(03)		14.83(04)			Dut	1.4
10/8/96	50305.43	40.9			15.31(03)	14.95(02)				EF1	1.4
18/8/96	50313.35	48.9	16.09(05)	16.22(03)	15.79(03)	15.41(03)	15.29(02)			Dut	2.3
1/9/96	50327.37	62.9			16.30(03)					EF1	1.5
5/9/96	50331.33	66.8	17.11(06)	17.14(05)	16.48(03)	16.02(04)	15.86(03)			EF2	2.1
1/10/96	50357.27	92.8			18.33(05)	17.76(04)	17.29(03)	17.13(03)		DF	1.5
8/10/96	50363.12	98.6	18.34(06)	18.50(05)	17.99(03)	17.50(03)	17.35(03)			EF2	2.5
24/10/96	50379.06	114.6	18.63(08)	18.65(07)	18.12(04)	17.64(05)	17.47(04)			Dut	2.5
28/10/96	50383.13	118.6	18.71(07)	18.78(05)	18.24(04)	17.75(04)	17.60(04)			Dut	1.4
18/11/96	50405.02	140.5			19.22(04)					EF1	1.4
18/11/96	50405.08	140.6	19.44(06)	19.66(05)	19.24(04)	18.46(04)	18.36(04)			Dut	1.5
1/12/96(*)	50418.15	153.6						18.45(20)	18.33(20)	IR2	0.7
13/12/96	50430.00	165.5		19.56(05)	18.97(03)	18.39(03)	18.25(03)			EF2	2.0
1/2/97	50480.05	215.6			19.68(05)	18.85(04)				Dut	1.5
13/5/97	50581.41	316.9	20.92(09)	20.85(05)	20.39(05)	19.43(05)	19.69(04)			EF2	1.5
14/5/97	50582.35	317.9			20.41(06)	19.46(06)				EF2	1.4
15/6/97	50614.54	350.0			20.20(06)	19.34(06)				DF	1.8
9/8/97	50669.40	404.9		20.71(09)	20.26(08)	19.46(06)	19.83(06)			DF	1.7
16/9/97	50708.00	443.5						19.05(20)	19.11(20)	IR2	1.2
17/9/97	50709.00	444.5						18.92(20)	19.08(20)	IR2	1.1
22/9/97	50713.17	448.7	21.01(20)	20.80(10)	20.43(08)	19.52(09)	19.92(08)			EF2	1.4
23/9/97	50714.13	449.6				19.66(10)				EF2	1.3
6/10/97	50726.07	461.6		20.75(10)	20.54(09)	19.72(08)	20.05(08)			Dut	1.3
12/10/97	50732.02	467.5			20.66(08)	19.74(07)				DF	1.7
17/11/97	50769.70	505.2						19.54(30)		IR2	0.9
5/12/97	50787.08	522.6		21.59(10)	21.38(07)	20.31(07)	20.69(08)			DF	1.4
2/1/98	50815.08	550.6			21.58(20)	20.59(10)	20.90(10)			Dut	1.5
3/1/98	50816.18	551.6			21.56(10)					Dut	1.6
4/1/98	50817.10	552.6			21.67(15)	20.54(10)				Dut	1.5
5/1/98	50818.05	553.6						20.40(40)		IR2	0.7
29/5/98	50962.42	697.9		22.83(20)	22.51(10)	21.38(10)				EF2a	1.4
30/5/98	50963.40	698.9				21.39(10)				EF2a	1.0
5/7/98	50999.41	734.9				21.48(10)				Dut	1.8
12/9/98	51068.80	804.3				21.99(10)				EF2a	1.1

(†) epoch relative to  $V_{max}$  occurred on MJD=50265(\*) for this epoch we give also  $K=17.68(20)$ 

Dut = Dutch+CCD camera; pixel scale=0.44"/px

Den = ESO1.0m+DENIS; pixel scale=3"/px

EF1 = ESO3.6m+EFOSC1; pixel scale =0.61"/px

EF2 = MPI2.2m+EFOSC2; pixel scale =0.34"/px

DF = D1.54m+DFOSC; pixel scale =0.39"/px

IR2 = MPI2.2m+IRAC2; pixel scale =0.28"/px

EF2a= ESO3.6m+EFOSC2; pixel scale =0.157"/px

**Table A2.** Spectroscopic observations of SN 1996al.

date	MJD	phase* (days)	range (Å)	tel.**	res. (Å)
23/7/96	50287.54	23	4400-7000	B&C	4
24/7/96	50288.39	24	4400-7000	B&C	4
25/7/96	50289.34	25	4400-7000	B&C	4
26/7/96	50290.34	26	4400-7000	B&C	4
29/7/96	50293.35	29	4030-9720	B&C	9
30/7/96	50294.34	30	4030-9720	B&C	9
31/7/96	50295.35	31	4030-9720	B&C	9
1/8/96	50296.38	32	4030-9720	B&C	9
7/8/96	50302.44	38	3740-6930	EF1	16
8/8/96	50303.44	39	3740-6930	EF1	16
9/8/96	50304.43	40	3740-6930	EF1	16
10/8/96	50305.43	41	3740-9890	EF1	16
12/8/96	50307.41	43	4940-6930	B&C	3
22/8/96	50317.16	53	3490-11080	B&C	13
1/9/96	50327.38	63	3730-6910	EF1	16
5/9/96	50331.38	67	3200-9250	EF2	10
10/9/96	50336.15	72	3520-10320	B&C	13
1/10/96	50357.29	93	3300-9050	DF	11
7/10/96	50363.30	99	5160-9270	EF2	11
7/10/96	50363.30	99	3430-10080	EF2	25
9/10/96	50365.51	101	5430-8890	RGO	8
19/11/96	50406.03	142	3730-6910	EF1	16
13/12/96	50430.12	166	3840-7990	EF2	12
30/4/97	50568.40	304	3600-9600	B&C	12
14/5/97	50582.35	318	5220-9250	EF2	11
10/8/97	50670.19	406	5100-10170	DF	12
22/9/97	50713.73	449	3500-9300	EF2	10
8/10/97	50729.07	465	3350-10040	B&C	12
11/10/97	50732.07	468	3400-8740	DF	12
5/12/97	50787.12	523	3500-8990	DF	11
29/5/98	50962.91	698	3380-7500	EF2a	18
12/9/98	51068.33	804	3320-7500	EF2a	18
27/7/01	52117.28	1853	4180-8180	FOR1	14
16/6/02	52441.31	2177	4090-9630	FOR1	10
23/7/04	53209.30	2944	4220-9630	FOR2	10
08/12/07	54442.04	4178	3900-9600	FOR2	10
11/10/09	55115.04	4850	3500-24000	XS	1,0.8,2.8
3/9/11	55807.07	5542	3500-24000	XS	1,0.8,2.8

\* - relative to the estimated epoch of  $V$  maximum (MJD=50265)

\*\* - See note to Table A1 for telescope coding plus:

B&C = ESO1.52m+B&C

RGO = AAT+RGO

FOR1 = ESO-VLT+FOR1

FOR2 = ESO-VLT+FOR2

XS = ESO-VLT+XShooter

The resolutions of XS refer to the 3 arms at 5000, 6000 and 15000 Å, respectively

## A2 Spectral line parameters of SN 1996al

**Table A3.** Spectral lines parameters as derived from spectra of SN 1996al up to 100 days.

phase (days)		H $\alpha$			He I 6678	He I 7065
		(Em) <sub>b</sub>	(Ab) <sub>n</sub>	(Em) <sub>n</sub>		
+23	$\lambda_c$ (Å)	6564	6556	6566		
	FWHM; $V_{I_0}^{blue}$ (km/s)	6500;12200	1050	400		
	$\phi^*$	372	-35	93		
+24	$\lambda_c$ (Å)	6568	6557	6566		
	FWHM; $V_{I_0}^{blue}$ (km/s)	6600;12700	930	390		
	$\phi^*$	477	-41	107		
+25	$\lambda_c$ (Å)	6567	6556	6565		
	FWHM; $V_{I_0}^{blue}$ (km/s)	6600;12800	970	380		
	$\phi^*$	482	-43	103		
+26	$\lambda_c$ (Å)	6566	6556	6566		
	FWHM; $V_{I_0}^{blue}$ (km/s)	7000;12700	990	410		
	$\phi^*$	513	-40	99		
+29	$\lambda_c$ (Å)	6566	6551	6565		7065
	FWHM; $V_{I_0}^{blue}$ (km/s)	6800;10300	1030	290		10600
	$\phi^*$	560	-29	75		70
+30	$\lambda_c$ (Å)	6565	6551	6565		7065
	FWHM; $V_{I_0}^{blue}$ (km/s)	6900;12600	1020	350		10800
	$\phi^*$	546	-30	73		59
+31	$\lambda_c$ (Å)	6565	6551	6565		7065
	FWHM; $V_{I_0}^{blue}$ (km/s)	6400;13100	970	310		9600
	$\phi^*$	446	-25	54		59
+32	$\lambda_c$ (Å)	6565	6550	6565		7065
	FWHM; $V_{I_0}^{blue}$ (km/s)	6500;11900	1020	300		10200
	$\phi^*$	482	-27	54		64
+38	$\lambda_c$ (Å)	6572	6554	6565		
	FWHM; $V_{I_0}^{blue}$ (km/s)	6300;12200	550	450		
	$\phi^*$	503	-32	71		
+39	$\lambda_c$ (Å)	6567	6553	6566		
	FWHM; $V_{I_0}^{blue}$ (km/s)	5400;11500	940	680		
	$\phi^*$	471	-37	41		
+40	$\lambda_c$ (Å)	6565	6548	6563		7065
	FWHM; $V_{I_0}^{blue}$ (km/s)	5800;11200	580	620		10600
	$\phi^*$	523	-26	39		55
+41	$\lambda_c$ (Å)	6568	6549	6567		
	FWHM; $V_{I_0}^{blue}$ (km/s)	5600;12000	530	680		
	$\phi^*$	511	-21	33		
+43	$\lambda_c$ (Å)	6569	6557	6566	6699	
	FWHM; $V_{I_0}^{blue}$ (km/s)	5700;11800	930	470	5100	
	$\phi^*$	440	-36	51	29	
+53	$\lambda_c$ (Å)	6568	6555	6565	6712	7035
	FWHM; $V_{I_0}^{blue}$ (km/s)	5700;10200	870	860	3600	10200
	$\phi^*$	209	-30	66	22	37
+63	$\lambda_c$ (Å)	6570	6556	6565	6699	
	FWHM; $V_{I_0}^{blue}$ (km/s)	5050;11000	810	940	3300	
	$\phi^*$	169	-28	63	16	



**Table A3** – *continued* Spectral lines parameters as derived from spectra of SN 1996al up to 100 days.

phase (days)		H $\alpha$			He I 6678	He I 7065
		(Em) <sub>b</sub>	(Ab) <sub>n</sub>	(Em) <sub>n</sub>		
+67	$\lambda_c$ (Å)	6570	6557	6566	6700	7067
	FWHM;V <sub>I<sub>0</sub></sub> <sup>blue</sup> (km/s)	4700;11100	850	650	3250	5500
	$\phi^*$	148	-23	38	11	13
+72	$\lambda_c$ (Å)	6568	6558	6567	6687	7059
	FWHM;V <sub>I<sub>0</sub></sub> <sup>blue</sup> (km/s)	4400;10200	1000	560	3700	4200
	$\phi^*$	123	-18	28	16	11
+93	$\lambda_c$ (Å)	6563	6560	6566	6673	7065
	FWHM;V <sub>I<sub>0</sub></sub> <sup>blue</sup> (km/s)	3500;8700	430	230	3300	3300
	$\phi^*$	82	-10	11	7	6
+99	$\lambda_c$ (Å)	6562	6557	6565	6667	7061
	FWHM;V <sub>I<sub>0</sub></sub> <sup>blue</sup> (km/s)	3200;10400	570	460	3300	3700
	$\phi^*$	85	-8	6	9	6
+101	$\lambda_c$ (Å)	6562	6554	6564	6673	
	FWHM;V <sub>I<sub>0</sub></sub> <sup>blue</sup> (km/s)	3250;10600	200:	450	3600	
	$\phi^*$	90	-7	3	95	

\* In units of  $\times 10^{-15}$  erg s<sup>-1</sup> cm<sup>-2</sup>; not corrected for reddening.

H $\alpha$  broad component better fitted with lorentzians up to phase +43d; after this phase they are better fitted with Gaussians. He I lines always fitted with Gaussians.

The velocities have been de-convolved for spectral resolution of each spectrum (see Table A2).

Estimated errors: wavelength position:  $\sim \pm 1\text{\AA}$  for narrow lines;  $\lesssim \pm 10\text{\AA}$  for broad lines; FWHM:  $\sim \pm 90$  km s<sup>-1</sup> for the narrow lines,  $\lesssim \pm 500$  km s<sup>-1</sup> for broad lines;  $\phi$ :  $\sim 1\text{-}2\%$  for narrow lines,  $\lesssim 10\%$  for broad lines.

**Table A4.** Spectral line parameters as derived from spectra of SN 1996al observed after 100 days.

phase (days)		H $\alpha$			He I6678	He I7065
		$B_{comp}$	$C_{comp}$	$R_{comp}$		
+142	$\lambda_c$ ( $\text{\AA}$ )	6539	6569	6597	6656	
	FWHM; $V_{I_0}^{blue}$ (km/s)	850;7800	950	970	4600	
	$\phi^*$	30	26	9	3	
+166	$\lambda_c$ ( $\text{\AA}$ )	6542	6570	6595	6678	7071
	FWHM; $V_{I_0}^{blue}$ (km/s)	730;6130	680	1340	2500	1800
	$\phi^*$	30	21	17	4	3
+304	$\lambda_c$ ( $\text{\AA}$ )	6542	6570	6594	6685	7064
	FWHM; $V_{I_0}^{blue}$ (km/s)	690;3900	800	630	1950	1200
	$\phi^*$	11	11	6	1.5	1.3
+318	$\lambda_c$ ( $\text{\AA}$ )	6542	6569	6593	6679	7066
	FWHM; $V_{I_0}^{blue}$ (km/s)	580;3800	880	670	1100	950
	$\phi^*$	12	16	7	1.0	1.5
+406	$\lambda_c$ ( $\text{\AA}$ )	6546	6573	6595	6684	7070
	FWHM; $V_{I_0}^{blue}$ (km/s)	550;3400	860	680	930	800
	$\phi^*$	8	15	7	3.1	4.5
+449	$\lambda_c$ ( $\text{\AA}$ )	6544	6570	6592	6680	7068
	FWHM; $V_{I_0}^{blue}$ (km/s)	510;3200	920	650	850	830
	$\phi^*$	7	16	7	3.1	5.2
+468	$\lambda_c$ ( $\text{\AA}$ )	6545	6571	6592	6681	7068
	FWHM; $V_{I_0}^{blue}$ (km/s)	520;2700	1050	720	950	800
	$\phi^*$	5.5	13	7	2.3	3.7
+523	$\lambda_c$ ( $\text{\AA}$ )	6546	6572	6593	6682	7071
	FWHM; $V_{I_0}^{blue}$ (km/s)	520;2400	930	580	980	860
	$\phi^*$	5	9	4	0.9	1.6
+698	$\lambda_c$ ( $\text{\AA}$ )	6549	6574	6597	6676	7071
	FWHM; $V_{I_0}^{blue}$ (km/s)	640;2100	860	630	780	860
	$\phi^*$	2.3	2.2	1.4	0.1:	0.2:
+804	$\lambda_c$ ( $\text{\AA}$ )	6546	6573	6598		
	FWHM; $V_{I_0}^{blue}$ (km/s)	640;1600	1090	720		
	$\phi^*$	1.0	1.5	0.8		
+1853	$\lambda_c$ ( $\text{\AA}$ )	6549	6577	6596		
	FWHM; $V_{I_0}^{blue}$ (km/s)	640;1500	820	< 630		
	$\phi^*$	0.9	0.6	0.2		
+2177	$\lambda_c$ ( $\text{\AA}$ )	6550	6577	6594		
	FWHM; $V_{I_0}^{blue}$ (km/s)	960;1700	590	590		
	$\phi^*$	0.25	0.05	0.03		
+2944	$\lambda_c$ ( $\text{\AA}$ )	6552	6577	6593		
	FWHM; $V_{I_0}^{blue}$ (km/s)	770;2400	680	630		
	$\phi^*$	0.10	0.02	0.01		
+4178	$\lambda_c$ ( $\text{\AA}$ )	6551	6577	6593		
	FWHM; $V_{I_0}^{blue}$ (km/s)	680;2200	680	630		
	$\phi^*$	0.13	0.02	0.006		

**Table A4** – *continued* Spectral line parameters as derived from spectra of SN 1996al observed after 100 days.

phase (days)		H $\alpha$			He I6678	He I7065
		B <sub>comp</sub>	C <sub>comp</sub>	R <sub>comp</sub>		
+4850	$\lambda_c$ (Å)	6552	6582	6599		
	FWHM; $V_{I_0}^{blue}$ (km/s)	960;1300	680	180		
	$\phi^*$	0.13	0.03	0.01		
+5542	$\lambda_c$ (Å)	6552	6575	6585		
	FWHM; $V_{I_0}^{blue}$ (km/s)	1000;1500	320	140		
	$\phi^*$	0.12	0.02	0.01		

\* In units of  $\times 10^{-15}$  erg s $^{-1}$  cm $^{-2}$ ; not corrected for reddening.

H $\alpha$  components better fitted with Lorentzians up to phase +523d; after this phase the H $\alpha$  components are better fitted with Gaussians. He I lines always fitted with Gaussians.

The FWHMs have been de-convolved for spectral resolution of each spectrum (see Table A2).

Estimated errors: wavelength position: about  $\pm 1\text{\AA}$  for narrow lines, up to about  $\pm 10\text{\AA}$  for broad lines; FWHM: about  $\pm 90$  km s $^{-1}$  for the narrow lines, up to about  $\pm 500$  km s $^{-1}$  for the broadest lines;  $\phi$ : about 1-2 % for narrow lines, up to  $\sim 10\%$  for the broad lines.